Journal of Geophysical Research: Solid Earth

RESEARCH ARTICLE
10.1029/2018JB015669

Fully Dynamic Spontaneous Rupture Due to Quasi-Static Pore Pressure and Poroelastic Effects: An Implicit Nonlinear Computational Model of Fluid-Induced Seismic Events

Lei Jin[1] **and Mark D. Zoback**[1]

[1]Department of Geophysics, Stanford University

Key Points:
- A new full-physics model of fluid-induced fully dynamic and spontaneously rupturing earthquake is introduced
- A new numerical modeling framework including discretization, linearization, and physics-based nonstationary preconditioning is presented
- Fully coupled poroelastic models can lead to notably different predictions on earthquake nucleation, dynamic rupture, and wavefields than decoupled models

Supporting Information:
- Supporting Information S1
- Movie S1
- Movie S2
- Movie S3
- Movie S4
- Movie S5
- Movie S6
- Movie S7
- Movie S8
- Movie S9
- Movie S10
- Movie S11
- Movie S12
- Movie S13
- Movie S14
- Movie S15
- Movie S16

Correspondence to:
L. Jin,
leijin@stanford.edu

Citation:
Jin, L., & Zoback, M. D. (2018). Fully dynamic spontaneous rupture due to quasi-static pore pressure and poroelastic effects: An implicit nonlinear computational model of fluid-induced seismic events. *Journal of Geophysical Research: Solid Earth*, *123*. https://doi.org/10.1029/2018JB015669

Received 20 FEB 2018
Accepted 2 OCT 2018
Accepted article online 6 OCT 2018

Abstract Fluid perturbations play a pivotal role in triggering earthquakes. However, the role of fluid in the coseismic rupture process remains largely unknown. To this end, we develop a 2-D fully dynamic spontaneous rupture model for fluid-induced earthquakes. The effect of fluid in the preseismic quasi-static regime is modeled as either pore pressure diffusion or fully coupled poroelasticity, using our Jin and Zoback (2017, https://doi.org/10.1002/2017JB014892) computational model. The two approaches lead to radically different predictions on the time of earthquake nucleation. Correspondingly, the evolved fluid pressure or poroelastic stress on the fault, together with the spatially altered density of the fluid-saturated hosting rock, is passed to the dynamic regime. Under the assumption of an undrained coseismic fluid-solid system, we discretize the fully dynamic Cauchy equation of motion subjected to an exact fault contact constraint using a split-node finite element method in space and an implicit Newmark family finite difference method in time. Within each time step, a fully implicit Newton-Raphson scheme is implemented iteratively for linearizing the fully discrete equations. Within each Newton iteration, a physics-based and nonstationary preconditioner is designed to accelerate the convergence of the selected generalized minimal residual method iterative linear solver. The effect of fluid is highlighted throughout the discretization and computational procedures. Finally, by conducting a numerical experiment, we illustrate that a fully coupled poroelastic model can lead to significantly different predictions on coseismic rupture behaviors and wavefields compared to a decoupled model. Our computational model can also serve as one of the earliest full-physics modeling tool for fluid-induced earthquakes.

1. Introduction

It is widely recognized that earthquakes over a wide range of scales have been induced by fluid injection into (or removal from) the subsurface. Thorough reviews are available on cases related to waste water disposal and hydraulic fracturing (Ellsworth, 2013), hydrocarbon extraction (Suckale, 2009), geothermal reservoir stimulation (Majer et al., 2007), and CO_2 sequestration (Zoback & Gorelick, 2015).

Given the orientation and the static frictional strength of a preexisting fault embedded within a fluid-filled porous medium subjected to a full in situ stress tensor, the mechanism of fluid inducing earthquakes is controlled by how the fluid overpressure alters the solid stress on the fault. There are currently two approaches to resolve this fluid effect. The first approach considers a fluid–solid decoupled process, in which the normal stress on the fault decreases by the amount of fault zone pressure according to the well-known Terzaghi effective stress law, whereas the shear stress on the fault remains constant (e.g., Byerlee, 1978; Mukuhira et al., 2017; Scuderi & Collettini, 2016; Walsh & Zoback, 2016). Interestingly, seismicity has been observed outside the region subjected to direct fluid perturbations (e.g., Megies & Wassermann, 2014; Stark & Davis, 1996; Yeck et al., 2016). Even within the perturbed region, pressure depletion sometimes also induces seismicity (Zoback & Zinke, 2002). Such observations motivate the use of a second approach that considers a fluid-solid coupled process and is typically discussed in the framework of Biot's theory of linear poroelasticity (Biot, 1941; Wang, 2000). Some classic configuration-specific analytical solutions of pressure and stress have been derived for studying earthquake triggering in response to fluid perturbations in an isotropic, homogenous, and linearly elastic porous medium (Altmann et al., 2014; Segall, 1985; Segall & Fitzgerald, 1998; Segall et al., 1994; Segall & Lu, 2015). There is also an increasing body of hypothetical or site-specific numerical case studies of earthquake triggering (e.g., Chang & Segall, 2016a, 2016b; Chang & Segall, 2017; Deng et al., 2016; Fan et al., 2016; Murphy et al., 2013; Zbinden et al., 2017). At a smaller scale,

numerical studies on fluid-induced microseismicity, typically motivated by the stimulation of hydrocarbon and geothermal reservoirs, have been reported. The same idea is used: the fluid effect is resolved, in either decoupled or coupled manners, and the grid-wise stress state is used to determine the occurrence of a microseismic event (e.g., Baisch et al., 2010; Maillot et al., 1999; Wassing et al., 2014). Such modeling can provide a synthetic microseismic catalog containing event source time, location, and even stress drop and moment magnitude, which offers some insights into event spatial-temporal and statistical characteristics and their relation to model inputs (Goertz-Allmann & Wiemer, 2012). The synthetic catalog can also be compared against laboratory and field observations for calibration of model physics, including, for example, medium rheology (Heinze et al., 2015), effects of stress transferring (Catalli et al., 2016; Rinaldi & Nespoli, 2017), and effects of poroelastic coupling (Riffault et al., 2016).

The above studies, regardless of the scale of induced seismicity, are concerned with the preseismic quasi-static triggering process only. Fault slip is not modeled (except for Maillot et al. (1999)), in part due to the fact that these models are cast in a continuum framework: faults are represented either implicitly as stochastic properties or explicitly as equal-dimensional entities with a rheology different from the hosting rock. To capture fault slip of an induced earthquake, one needs to build numerical tools capable of handling discontinuities. An emerging alternative to traditional approaches is to model the medium as individual particles bonded together at points of contact. This approach naturally accommodates arbitrary geometries of discontinuities at a microscale; the governing laws are typically discretized and solved using the popular Particle Flow Code (Itasca Consulting Group, 1999). This technique was initially employed to simulate microseismicity in dry brittle rocks (Hazzard & Young, 2004) and then extended to study fluid-induced microseismicity (Raziperchikolaee et al., 2014; Yoon et al., 2014; Zhao & Young, 2011). Compared to the previously mentioned modeling, this technique provides additional information on source mechanisms like seismic moment tensors.

In the above class of models, however, the fault slip is given as a static solution, and its calculation does not involve fault friction. As a step forward, a model has recently been proposed that considers both fluid perturbations and slip on explicit faults with constant friction; an extended finite volume method is developed for space discretization of both the fluid and the solid (Deb & Jenny, 2017a; Deb & Jenny, 2017b). Unfortunately, the evolving fault frictional strength (such as slip weakening or rate-and-state friction) is not included. To this end, a handful of physically more representative models of induced earthquakes have been developed by considering fluid perturbations, fault slip, and slip-dependent fault friction simultaneously. Among these studies, some resolve the fluid effect in a decoupled manner by solving a separate fluid diffusion equation and inserting the resulting fluid pressure into an established earthquake rupture model (e.g., Dieterich et al., 2015; Galis et al., 2017; Garagash & Germanovich, 2012; Kroll et al., 2017; Richards-Dinger & Dieterich, 2012; Viesca & Rice, 2012). Others follow a coupled approach to account for the fluid effect. For example, McClure and Horne (2011) developed a model of slip flow on a single isolated but hydraulically conductive fault embedded in an essentially impermeable hosting rock. Jha and Juanes (2014) formulated a more comprehensive multiphase poromechanical framework that permits fault slip simultaneously. In terms of space discretization, for the solid, the former uses the boundary element method whereas the latter directly uses Pylith (Aagaard et al., 2013), which employs a split-node finite element method; for the fluid, both models opted for the finite volume method, in particular, the latter uses General Purpose Research Simulator (Cao, 2002); in terms of coupling, both models advance the coupled solution in time in a sequential manner. We point out that former model, motivated by fracture stimulation in tight reservoirs, assumed fluid perturbations only within the fault and is less appropriate for general fluid-induced earthquakes; additionally, it is the fault pressure rather than the fault poroelastic stress that is passed from the fluid problem to the solid problem, so the model is essentially fluid-to-solid decoupled. Recently, applications to induced seismicity of the former were reported by, for example, Gischig (2015) and Norbeck and Horne (2016) and of the latter model by Juanes et al. (2016) and Cueto-Felgueroso et al. (2017).

One common assumption made in the aforementioned models (except for Galis et al. (2017)) is that the induced fault slip is quasi-dynamic as opposed to fully dynamic. The quasi-dynamic approach approximates the inertial response of the fault via a radiation damping term in the fault shear traction (Rice, 1993; Rice & Ben-Zion, 1996). This approach is known to have certain limitations. For example, dynamic changes are instantaneous rather than at wave speeds; in some parts of the parameter space, predictions are qualitatively different than those given by a fully dynamic model (e.g., Thomas et al., 2014). Additionally, these models do not

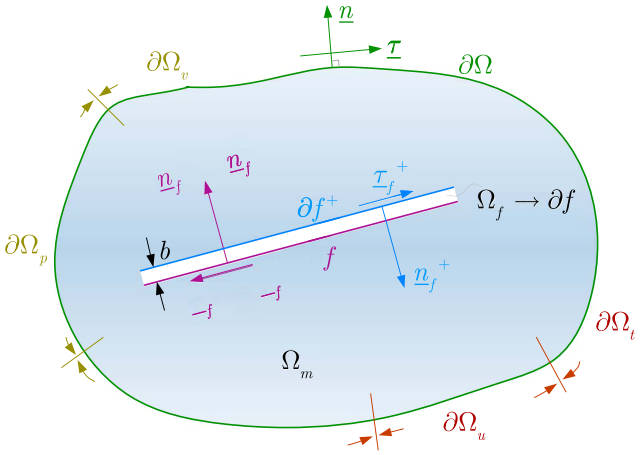

Figure 1. Schematic illustration of the porous matrix domain Ω_m embedded with a fault Ω_f with an aperture b. b is vanishingly small such that the fault can be represented as an internal discontinuity for computational purposes. The two fault surfaces are denoted as ∂f^+ and ∂f^-, with their respective unit normal and tangential vectors denoted as $\underline{n}_f^+$, $\underline{\tau}_f^+$, and $\underline{n}_f^-$, $\underline{\tau}_f^-$; the latter two are selected as the fault normal and tangential unit vectors, that is, $\underline{n}_f := \underline{n}_f^-$, $\underline{\tau}_f := \underline{\tau}_f^-$. The whole domain Ω is externally bounded by $\partial\Omega$ that is associated with unit normal and tangential vectors $\underline{n}$ and $\underline{\tau}$. The Dirichlet and Neumann boundaries are denoted as $\partial\Omega_p$ and $\partial\Omega_v$ for the fluid problem, and as $\partial\Omega_u$ and $\partial\Omega_t$ for the solid problem, respectively. For a boundary value problem in general, $\partial\Omega_p \cap \partial\Omega_v = \emptyset$, $\partial\Omega_p \cup \partial\Omega_v = \partial\Omega$; $\partial\Omega_u \cap \partial\Omega_t = \emptyset$, $\partial\Omega_u \cup \partial\Omega_t = \partial\Omega$, and $\partial\Omega_p \neq \emptyset$, $\partial\Omega_u \neq \emptyset$. Specific to the elastodynamic rupture problem, however, $\partial\Omega$ can be replaced with an absorbing boundary and a null $\partial\Omega_u$ is permissible.

provide an opportunity to examine the seismic radiation patterns, wave propagation, and waveforms that might be characteristic of fluid-induced earthquakes, as have been documented by some recent studies (Cesca et al., 2013; Gritto & Jarpe, 2014); they also do not produce the associated dynamic signals typically used as proxies in quantitative risk assessment of induced seismicity (Atkinson, 2015). Along this line, Duan (2016) applied a fully dynamic rupture model to induced seismicity; there the fluid effect arises not from external sources (e.g., injection) but rather the coseismic slip. Cappa and Rutqvist (2012) provided a more relevant study where they first solved a coupled quasi-static poroelastic equation iteratively using two existing codes and then directly used the stress state at the onset of failure as an input for the dynamic wave modeling. Similar work is presented by Buijze et al. (2017). Lastly, we also mention a code that offers both poroelastic and elasto-dynamic modules, suitable for solving a coupled injection problem and a dynamic rupture problem, respectively (Ali, 2014; Meng, 2017). Unfortunately, discontinuity is not included in the first module, and no link was established between these two modules.

Fluid-induced earthquakes encompass both preseismic quasi-static triggering and coseismic fully dynamic spontaneous rupture under a dynamically evolving fault strength. The transition from the quasi-static regime to the dynamic regime is marked in time by the onset of rupture and in space by the location of nucleation of rupture. More importantly, the fluid effect from the former process, regardless of being resolved in a decoupled manner or a coupled manner, significantly impacts the latter process. First, it alters the fault stress, which is known to have a fundamental control over the rupture style, rupture velocity, and wave propagation (e.g., Ampuero & Ben-Zion, 2008; Andrews, 1976; Ben-David et al., 2010; Dunham, 2007; Gabriel et al., 2012). Second, it modifies the density of the medium, and therefore must be taken into account for a dynamic problem with inertia. There seem to be few studies addressing these issues. This motivates us to develop a general computational model of fluid-induced earthquakes as a tool to study fault rupture in relation to fluid perturbations. To the best of our knowledge, this work presents one of the earliest models of fully dynamic spontaneous earthquake rupture triggered by external fluid perturbations, especially in a poroelastically coupled manner and is intended to investigate fluid-induced earthquakes.

The organization of the paper is as follows. In section 2, we outline governing equations of (1) preseismic quasi-static loading due to external fluid perturbations, (2) coseismic fully dynamic spontaneous rupture, and (3) the transitional criterion; we close the system with constraints on the fault together with boundary and initial conditions. The numerical formulation and the computational procedures related to the quasi-static subproblem were detailed in Jin and Zoback (2017). We therefore focus only on the dynamic regime in the rest of the paper. Section 3 describes the numerical formulation and the space-time discretization. The contact constraint on the fault is imposed exactly via the Lagrangian multiplier method, leading to a saddle-point structure of the fully discrete form that is challenging to solve. The use of an implicit time-stepping scheme renders the system nonlinear, and the linearization procedure is given in section 4. The construction of a discrete Lagrangian space obeying the inf-sup stability constraint is addressed in section 5. Section 6 discusses solver section and highlights the development of a novel physics-based nonstationary preconditioner for accelerating the convergence. A numerical example highlighting the impact of the fluid effect on fault rupture is provided in section 7. Finally, a summary and some conclusions are provided in section 8.

2. Problem Statement

2.1. Model Domain and Boundary

We hereinafter restrict our focus on a 2-D in-plane problem. Consider an arbitrary domain $\Omega = \Omega_f \cup \Omega_m$, where $\Omega_f \subset \mathbb{R}^2$ indicates a fault domain and $\Omega_m \subset \mathbb{R}^2$, a porous matrix (hosting rock) domain, see Figure 1. Since the aperture of a fault is usually orders of magnitude lower than the typical mesh size of the matrix, for

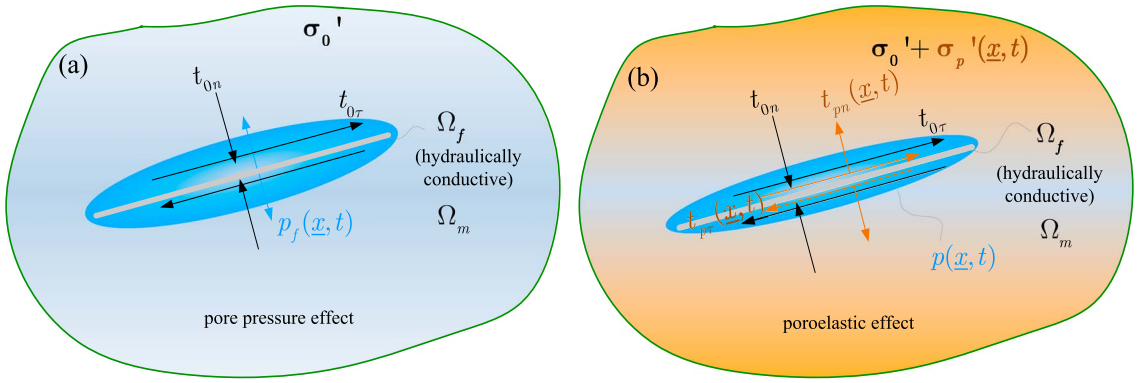

Figure 2. Graphic illustration of two ways to resolve the fluid effect in the quasi-static regime, including (a) a fluid-solid decoupled approach resolving the pore pressure effect, (b) a fluid-solid coupled approach resolving the poroelastic effect. In Figures 2a and 2b, both the Ω_m and the Ω_f are hydraulically conductive; the Ω is subjected to an initial effective stress field $\boldsymbol{\sigma}_0'$, and the associated fault normal and shear traction are denoted as t_{0n} and $t_{0\tau}$; the fluid pressure, denoted as $p(\underline{x},t)$ and colored with blue, increases on and near the fault, although its distribution can differ. In Figure 2a, only the fault fluid pressure, $p_f(\underline{x},t)=p(\underline{x},t)_{,x\in\Omega_f}$, is needed, modifying only the t_{0n}. In Figure 2b, a poroelastic stress field, denoted as $\boldsymbol{\sigma}_p'(\underline{x},t)$ and colored with yellow, is generated throughout the domain due to the full coupling between $\boldsymbol{\sigma}_p'(\underline{x},t)$ and $p(\underline{x},t)$, augmenting both the t_{0n} and the $t_{0\tau}$ by the amount of $t_{pn}(\underline{x},t)$ and $t_{p\tau}(\underline{x},t)$, respectively. In both Figures 2a and 2b, the density of the fluid-solid mixture changes in space and time.

computational purposes, we do not resolve the transversal details within the fault. Instead, we represent it as a reduced-dimensional internal discontinuity, $\Omega_f \rightarrow \partial f \subset \mathbb{R}^1$. The fault thickness will be implicitly accounted for during computation.

2.2. Pore Pressure Effect and Poroelastic Effect

We consider Ω to be initially saturated with a single-phase compressible fluid, and we shall restrict our focus only on cases where Ω_f is hydraulically conductive as opposed to sealing. Specific and pivotal to an appropriate model of fluid-induced seismic events is to resolve how the fluid perturbation modifies the fault stress, especially in the preseismic quasi-static regime. As has been introduced in section 1, this fluid effect can be resolved as either only pore pressure effect via a fluid-solid decoupled approach or as poroelastic effect via a fluid-solid fully coupled approach, as it is illustrated and compared in Figure 2.

2.3. Governing Equations

Our model is based on decomposing the physical process of an induced seismic event into two sequential subprocesses, including the preseismic quasi-static triggering subprocess and the coseismic dynamic rupture subprocess. Below we present the governing equations of each subprocess. The time at which the problem transitions from quasi-static to dynamic is denoted hereinafter as t^*.

2.3.1. Preseismic Quasi-Static Regime

We start by first discussing the fluid-solid coupled approach. The objective here is to calculate injection-induced space- and time-dependent changes in the fluid pressure and the solid stress relative to an initial reference state. This process is quasi-static and is governed by the Biot's theory of poroelasticity. The theory states that the fluid and solid are fully coupled: the gradient of the fluid pressure enters the force balance law as an equivalent body force, driving changes in the solid stress; the volumetric strain rate enters the mass conservation law as an equivalent external fluid source, driving changes in the fluid pressure. While many analytical and numerical solutions to this problem are available, the solution is challenging to find for a faulted porous medium due to fault-related complexities. Within the existing framework of Biot's theory of poroelasticity, Jin and Zoback (2017) recently proposed a fluid-solid fully coupled model for an arbitrarily faulted porous medium. The model demonstrates how the fluid storage capacity, the hydraulic conductivity, and the elastic stiffness of the system are modified and augmented due to the presence of faults and the additional sets of fluid and solid constitutive laws; domain interactions in the form of mass exchange and the nonlinearity due to pressure-dependent hydraulic aperture of faults are also resolved in the model. Here we use this model in this study but with one simplification. Specifically, in the original model, the matrix and the faults are governed by different solid constitutive laws even prior to the shear failure; however, here

the fault behaves the same as the rest of the domain. Without attempting to present the full details of the original model, here we outline the key governing equations.

First, the mass conservation law with solid-to-fluid coupling

$$\begin{aligned}&\left(\Lambda_0(\underline{x})\phi_{m0}(\underline{x})\left(C_m+C_\rho\right)+\left(1-\Lambda_0(\underline{x})\right)\phi_{f0}(\underline{x})\left(C_f+C_\rho\right)\right)\dot{p}(\underline{x},t)\\&-\alpha\nabla\cdot\dot{\underline{u}}_p(\underline{x},t)+\nabla\cdot\underline{v}(\underline{x},t)=s(\underline{x},t)\qquad\qquad\forall\underline{x}\in\Omega,t\le t^*\end{aligned}\tag{1}$$

and, second, the quasi-static force balance law with fluid-to-solid coupling,

$$\nabla\cdot\left(\boldsymbol{\sigma}_p^{'}(\underline{x},t)+\alpha p(\underline{x},t)\mathbf{1}\right)=\nabla\cdot\boldsymbol{\sigma}_p^{'}(\underline{x},t)+\alpha\nabla p(\underline{x},t)=\underline{0}\qquad\forall\underline{x}\in\Omega,t\le t*\tag{2}$$

where $p(\underline{x},t)$, $\underline{u}_p(\underline{x},t)$, and $\boldsymbol{\sigma}_p^{'}(\underline{x},t)$ are the injection-induced changes in the fluid pressure, the solid displacement vector, and the effective stress tensor, all relative to an initial reference state; $\Lambda_0(\underline{x})$ is the geometric parameter calculated from the initial fault-matrix configuration; $\phi_{m0}(\underline{x})$ and $\phi_{f0}(\underline{x})$ are the initial intrinsic porosity of the matrix and the fault (typically $\phi_{f0}(\underline{x})$=1); C_ρ, C_m, and C_f are the compressibility of the fluid, the matrix pores, and the fault, and they are material constants; $\underline{v}(\underline{x},t)$ is the fluid velocity; $s(\underline{x},t)$ is the external fluid source divided by the initial fluid density; α is the Biot-Willis coefficient quantifying the susceptibility of the solid to the fluid and vice versa, and $\mathbf{1}$ is unit identity.

Equations (1) and (2) are fully coupled and preferably solved simultaneously. Notice also the use of a compressive strain/stress positive notation, under which Jin and Zoback (2017) showed that the normal components of $\boldsymbol{\sigma}_p^{'}(\underline{x},t)$ are negative (extensional) immediately near a fault subjected to fluid pressure elevation, although compressive normal stress can develop further away from the fault.

In equation (1), $p(\underline{x},t)$ is related to $\underline{v}(\underline{x},t)$ via the following fluid constitutive laws, including a linear law for the porous matrix and a nonlinear law for the fault. They read

$$\underline{v}(\underline{x},t)=\begin{cases}-\eta^{-1}\mathbf{k}_m(\underline{x})\cdot\nabla p(\underline{x},t) & \forall\underline{x}\in\Omega_m\\ -\eta^{-1}\dfrac{1}{12}\left(b_0\left(1+C_f p_f(\underline{x},t)\right)\right)^2\nabla_\tau p_f(\underline{x},t) & \forall\underline{x}\in\partial f\times\left[-\dfrac{b}{2},\dfrac{b}{2}\right]\end{cases}\tag{3}$$

where η is the fluid viscosity, $\mathbf{k}_m$ is the matrix permeability tensor, b and b_0 are the fault hydraulic aperture and its initial value, and $p_f(\underline{x},t)\coloneqq p(\underline{x},t),\forall\underline{x}\in\Omega_f$ is the fluid pressure on the fault (Figure 2a); by assumption, $p_f(\underline{x},t)$ is continuous across the fault. The presence of the second equation in equation (3) renders the coupled system (equations (1) and (3)) nonlinear.

In equation (2), $\boldsymbol{\sigma}_p^{'}(\underline{x},t)$ is related to the displacement via the following drained linearly elastic solid constitutive law.

$$\boldsymbol{\sigma}_p^{'}(\underline{x},t)=\frac{\nu E}{(1+\nu)(1-2\nu)}\left(\nabla\cdot\underline{u}_p(\underline{x},t)\right)\mathbf{1}+\frac{E}{2(1+\nu)}\left[\nabla\underline{u}_p(\underline{x},t)+\left(\nabla\underline{u}_p(\underline{x},t)\right)^T\right]\quad\forall\underline{x}\in\Omega\tag{4}$$

where E and ν are the Young's modulus and the drained Poisson's ratio of the fluid-saturated solid.

The term *drained* here is in a local sense as opposed to a global sense; it indicates the presence of a relative velocity between the fluid and the solid within the domain (e.g., Borja & Koliji, 2009), rather than a more commonly used free fluid flux at the domain boundary.

When opting for the decoupled approach, one only needs to solve for the fluid overpressure $p(\underline{x},t)$ from the solid-to-fluid decoupled mass conservation law, which can be obtained by simply removing the solid volumetric strain rate term $-\nabla\cdot\dot{\underline{u}}_p(\underline{x},t)$ from equation (1). The fluid diffusion equation is then obtained by substituting in equation (3). The details are omitted.

2.3.2. Transition

We opt for the linear Mohr-Coulomb shear failure criterion for determining t^*. This requires the calculation of the fault Coulomb stress, denoted hereinafter as CS. Neglecting the fault cohesion, CS reads the following with pore pressure effect (Figure 2a):

$$\begin{aligned} CS(\underline{x},t) &= t_{0\tau} - \mu_s(t_{0n} - p_f(\underline{x},t)) \\ &= \left[\left\|\boldsymbol{\sigma}_0{}'\cdot\underline{n}_f\right\|^2 - \left(\boldsymbol{\sigma}_0{}' : \underline{n}_f\otimes\underline{n}_f\right)^2\right]^{\frac{1}{2}} - \mu_s\left(\boldsymbol{\sigma}_0{}' : \underline{n}_f\otimes\underline{n}_f - p_f(\underline{x},t)\right) \end{aligned} \tag{5}$$

and differently with poroelastic effect (Figure 2b) as

$$\begin{aligned} CS(\underline{x},t) &= t_{0\tau} + t_{p\tau}(\underline{x},t) - \mu_s\left(t_{0n} + t_{pn}(\underline{x},t)\right) \\ &= \left[\left\|\left(\boldsymbol{\sigma}_0{}' + \boldsymbol{\sigma}_p{}'(\underline{x},t)\right)\cdot\underline{n}_f\right\|^2 - \left(\left(\boldsymbol{\sigma}_0{}' + \boldsymbol{\sigma}_p{}'(\underline{x},t)\right) : \underline{n}_f\otimes\underline{n}_f\right)^2\right]^{\frac{1}{2}} - \mu_s\left(t_{0n} + \boldsymbol{\sigma}_p{}'(\underline{x},t) : \underline{n}_f\otimes\underline{n}_f\right) \end{aligned} \tag{6}$$

where the meanings of $t_{0\tau}$, t_{0n}, $t_{pn}(\underline{x},t)$, $t_{p\tau}(\underline{x},t)$, p_f, $\boldsymbol{\sigma}_0{}'$, and $\underline{n}_f$ are explained above, and μ_s is the static frictional coefficient of the fault. $t_{pn}(\underline{x},t)$ is expected to be negative following our sign convention. Note that while it is safe to calculate t_{0n} and $t_{pn}(\underline{x},t)$ separately from $\boldsymbol{\sigma}_0{}'$ and $\boldsymbol{\sigma}_p{}'(\underline{x},t)$, $t_{0\tau} + t_{p\tau}(\underline{x},t)$ must be calculated as a single variable by first superposing $\boldsymbol{\sigma}_0{}'$ and $\boldsymbol{\sigma}_p{}'(\underline{x},t)$ to account for possible changes in the sense of shear.

In either approach, we assume that dynamic rupture begins when the maximum Coulomb stress along the fault, defined as

$$CS_{max}(t) \coloneqq \max(CS(\underline{x},t)), \underline{x}\in\partial f \tag{7}$$

is driven from negative to 0. Therefore, t^* can be solved from the following:

$$CS_{max}(t*) = 0 \tag{8}$$

2.3.3. Coseismic Dynamic Regime

The objective here is to calculate the coseismic dynamic changes. Taking the coupled approach for example (coupling as in the quasi-static regime), the linear momentum is now conserved among the injection-induced changes at the onset of rupture and the slip-induced coseismic dynamic changes. Hence, we solve for the following fully dynamic Cauchy equation of motion:

$$\nabla\cdot\left(\boldsymbol{\sigma}_p{}'(\underline{x},t*) + \alpha p(\underline{x},t*)\mathbf{1} + \underbrace{\boldsymbol{\sigma}_s{}'(\underline{x},t) + \overbrace{\alpha p_s(\underline{x},t)\mathbf{1}}^{\text{undrained}}}_{\boldsymbol{\sigma}_s(\underline{x},t)}\right) = \rho_{mix}(\underline{x},t*)\,\ddot{\underline{u}}_s(\underline{x},t)\forall\underline{x}\in\Omega, t\geq t* \tag{9}$$

where $\boldsymbol{\sigma}_s{}'(\underline{x},t)$, $p_s(\underline{x},t)$, $\boldsymbol{\sigma}_s(\underline{x},t)$, and $\underline{u}_s(\underline{x},t)$ are slip-induced changes in the effective stress tensor, the pore pressure, the Cauchy total stress tensor, and the displacement vector, and $\rho_{mix}(\underline{x},t^*)$ is the density of the fluid-solid mixture (i.e., fluid-saturated solid) evaluated at t^*.

Equation (2) states that an initial balance has been reached through the quasi-static process; the first part is divergence free, and therefore, equation (9) reduces to

$$\nabla\cdot\boldsymbol{\sigma}_s(\underline{x},t) = \rho_{mix}(\underline{x},t*)\,\ddot{\underline{u}}_s(\underline{x},t)\forall\underline{x}\in\Omega, t\geq t* \tag{10}$$

Equation (10) states that the slip-induced dynamic perturbation only needs to rebalance itself in order for the fluid-solid mixture to regain equilibrium during the dynamic rupture, irrespective of whether the mixture is initially in quasi-static balance in a fluid-to-solid decoupled manner or a poroelastically coupled manner. Therefore, equation (10) applies in both approaches.

It is a common practice to consider the coseismic fluid-solid mixture as an undrained elasto-dynamic system, that is, no gain or loss of the pore fluid over the timescale relevant to the fault rupture (e.g., Duan, 2016; Wang & Barbour, 2017). This motivates the use of a so-called undrained Poisson's ratio (Cleary, 1977; Rice & Cleary, 1976) in a constitutive law reminiscent to that of an elastic solid for relating $\boldsymbol{\sigma}_s(\underline{x},t)$ as opposed $\boldsymbol{\sigma}_s{}'(\underline{x},t)$ to $\underline{u}_s(\underline{x},t)$ (e.g., Dunham & Rice, 2008; Viesca et al., 2008). Adapted to our notation, the same undrained constitutive law reads

$$\boldsymbol{\sigma}_s(\underline{x},t) = \frac{\nu_u E}{(1+\nu_u)(1-2\nu_u)}(\nabla\cdot\underline{u}_s(\underline{x},t))\mathbf{1} + \frac{E}{2(1+\nu_u)}\left[\nabla\underline{u}_s(\underline{x},t) + (\nabla\underline{u}_s(\underline{x},t))^T\right] \quad \forall\underline{x}\in\Omega \tag{11}$$

where ν_u is the undrained Poisson's ratio of the fluid-saturated solid.

In equations (9) and (10), ρ_{mix} is given by the following volume-weighted sum:

$$\rho_{\mathrm{mix}}(\underline{x},t*)=\overline{\Phi}(\underline{x},t*)\rho(\underline{x},t*)+\left(1-\overline{\Phi}(\underline{x},t*)\right)\rho_s \tag{12}$$

where $\rho(\underline{x},t^*)$ and ρ_s are the density of the fluid and the solid mineral, respectively, and $\overline{\Phi}(\underline{x},t^*)$ is the porosity of the fault-matrix system with the augmentation by the solid-to-fluid coupling effect, if considered. Both $\rho(\underline{x},t^*)$ and $\overline{\Phi}(\underline{x},t^*)$ are evaluated at t^*. $\rho(\underline{x},t^*)$ reads

$$\rho(\underline{x},t^*)=\rho_0\left(1+C_\rho p(\underline{x},t^*)\right) \tag{13}$$

where ρ_0 and C_ρ are the initial density and compressibility of the fluid.

$\overline{\Phi}(\underline{x},t^*)$ reads differently for the decoupled and couple approaches:

$$\overline{\Phi}(\underline{x},t*)=\begin{cases}\Phi(\underline{x},t*),\ \text{pore}\quad\text{pressure}\quad\text{effect}\\ \Phi(\underline{x},t*)-\alpha\nabla\cdot\underline{u}_p(\underline{x},t*),\ \text{poroelastic}\quad\text{effect}\end{cases} \tag{14}$$

and $\Phi(\underline{x},t^*)$ is the so-called partial porosity of the faulted porous medium; it is in a sense a *coalesced* porosity obtained from the matrix porosity and the fault porosity under a given configuration. When evaluated at t^*, it is calculated from the following expression using the fluid pressure at t^* (see Jin and Zoback (2017) for details):

$$\Phi(\underline{x},t^*)=\Lambda_0(\underline{x})\phi_{m0}(\underline{x})(1+C_m p(\underline{x},t^*))+(1-\Lambda_0(\underline{x}))\phi_{f0}(\underline{x})(1+C_f p(\underline{x},t^*)) \tag{15}$$

2.4. Coseismic Constraints on the Fault

Here we outline several constraints to be imposed on the fault for the subproblem in the dynamic regime. First, during fault slip, the normal component of the displacement across the fault remains continuous. This can be specified by imposing the following contact constraint over the full length of the fault:

$$(\underline{u}_s{}^+(\underline{x},t)-\underline{u}_s{}^-(\underline{x},t))\cdot\underline{n}_f=[\![\underline{u}_s(\underline{x},t)]\!]\cdot\underline{n}_f=0\qquad\forall\underline{x}\in\partial f,\ \ t\geq t^* \tag{16}$$

where $[\![\cdot]\!]:=(\cdot)|_{\Gamma^+}-(\cdot)|_{\Gamma^-}$ denotes a jump in a quantity across a discontinuity.

Second, we impose the traction continuity condition across the fault:

$$\underline{t}_s^+(\underline{x},t)+\underline{t}_s^-(\underline{x},t)=\underline{0}\quad\forall\underline{x}\in\partial f,\ \ t\geq t^* \tag{17}$$

Here $\underline{t}_s{}^{\pm}(\underline{x},t)$ is the slip-induced traction on the positive and negative sides of the fault. They read

$$\underline{t}_s^j(\underline{x},t)=\boldsymbol{\sigma}_s^j(\underline{x},t)\cdot\underline{n}_f{}^j,\ \ j=+,- \tag{18}$$

Define a slip-induced fault traction $\underline{t}_s(\underline{x},t)$ as the traction on the negative side of the fault:

$$\underline{t}_s(\underline{x},t):=\underline{t}_s^-(\underline{x},t)=-\underline{t}_s^+(\underline{x},t),\qquad\underline{x}\in\partial f,\ \ t\geq t^* \tag{19}$$

It can be then decomposed as

$$\underline{t}_s(\underline{x},t)=t_{sn}(\underline{x},t)\underline{n}_f+t_{s\tau}(\underline{x},t)\underline{\tau}_s \tag{20}$$

where t_{sn} and $t_{s\tau}$ are the slip-induced changes in the magnitude of the fault normal and shear traction, t_{sn} is also referred to hereinafter as the *contact pressure*, and $\underline{\tau}_s$ is the unit vector indicating the slip direction on the negative side, which can be determined from the following for a 2-D problem:

$$\underline{\tau}_s=\begin{cases}\underline{\tau}_f,\ if\ \left(\boldsymbol{\sigma}_0{}'+\boldsymbol{\sigma}_p{}'(\underline{x},t*)\right):\underline{n}_f\otimes\underline{\tau}_f>0\\ -\underline{\tau}_f,\ if\ \left(\boldsymbol{\sigma}_0{}'+\boldsymbol{\sigma}_p{}'(\underline{x},t*)\right):\underline{n}_f\otimes\underline{\tau}_f<0\end{cases} \tag{21}$$

Finally, for the frictional sliding along a cohesionless fault, a third condition, namely the consistency condition (e.g., Borja, 2013), also commonly known as the fault boundary condition (e.g., Allison & Dunham, 2017), is required. With pore pressure effect, it reads

$$t_{s\tau}(\underline{x},t) = \mu_f(t_{0n} - p_f(\underline{x},t) + t_{sn}(\underline{x},t)) - t_{0\tau}, \quad \underline{x}\in\partial f, t\geq t^* \tag{22}$$

and the following with poroelastic effect:

$$t_{s\tau}(\underline{x},t) = \mu_f\left(t_{0n} + t_{pn}(\underline{x},t^*) + t_{sn}(\underline{x},t)\right) - \left(t_{0\tau} + t_{p\tau}(\underline{x},t^*)\right), \quad \underline{x}\in\partial f, t\geq t^* \tag{23}$$

In equations (22) and (23), $t_{s\tau}(\underline{x},t)$ and $t_{sn}(\underline{x},t)$ are calculated from $\boldsymbol{\sigma}_s(\underline{x},t)$ in the same manner as is shown in equations (5) and (6), μ_f is a dynamically evolving fault frictional coefficient. Here we opt for the following well-known linear slip-weakening law (e.g., Andrews, 1976):

$$\mu_f(|\underline{s}(\underline{x},t)|) = \begin{cases} \mu_s - (\mu_s - \mu_d)\dfrac{|\underline{s}(\underline{x},t)|}{d_c}, & |\underline{s}(\underline{x},t)|\leq d_c \\ \mu_d, & |\underline{s}(\underline{x},t)| > d_c \end{cases}, \quad \underline{x}\in\partial f \tag{24}$$

where μ_d is the dynamic counterpart of μ_s shown in equations (5) and (6), $\underline{s}(\underline{x},t) \coloneqq \underline{u}_s^{\,+}(\underline{x},t) - \underline{u}_s^{\,-}(\underline{x},t), \underline{x}\in\partial f$ is the fault slip vector with a magnitude $|\underline{s}(\underline{x},t)|$, and d_c is the slip-weakening distance.

Due to the presence of equation (24), equation (10) is rendered highly nonlinear with respect to both the displacement $\underline{u}_s(\underline{x},t)$ and the contact pressure t_{sn}, both are the primary unknowns in this study (section 3). It is worth noting that while the coseismic dynamic rupture in the two approaches is essentially governed by the same conservation law (equation (10)) and the same constitutive law (equation (11)); because of the nonlinearity, the difference highlighted between equations (22) and (23) nonetheless will produce different results in the coseismic rupture. Numerically solving the nonlinear problem requires certain iterative linearization procedures (section 4), including deriving the Jacobian by taking the partial derivatives of the residual with respect to the unknowns. Since $\underline{u}_s(\underline{x},t)$ is one of the primary unknowns, we are motivated to further express μ_f directly as a function of $\underline{u}_s(\underline{x},t)$. To do so, we take advantage of the following trivial relationship between the displacement vectors on the two sides of the fault:

$$\underline{u}_s^{+}(\underline{x},t) = \gamma(\underline{x},t)\underline{u}_s^{-}(\underline{x},t) \tag{25}$$

where $\gamma(\underline{x},t)$ is a negative variable for a general (i.e., asymmetric) rupture problem. In the special case of symmetric rupture, $\gamma(\underline{x},t) \equiv -1$.

Therefore, the magnitude of the slip vector can be related to the magnitude of the displacement vector on either side of the fault via

$$|\underline{s}(\underline{x},t)| = \beta^j(\underline{x},t)\left|\underline{u}_s^j(\underline{x},t)\right|, \quad j = +,- \tag{26}$$

Here

$$\beta^j(\underline{x},t) = \begin{cases} 1-\gamma(\underline{x},t), & j = - \\ 1 - \dfrac{1}{\gamma(\underline{x},t)}, & j = + \end{cases} \tag{27}$$

Noticing equations (26) and (27), equation (24) can be rewritten as the following, which will soon prove useful in facilitating the derivation of Jacobian in section 4,

$$\mu_f\left(\left|\underline{u}_s^j(\underline{x},t)\right|\right) = \begin{cases} \left(1 - 2\alpha_f^j(\underline{x},t)\left|\underline{u}_s^j(\underline{x},t)\right|\right)\mu_s, & \left|\underline{u}_s^j(\underline{x},t)\right| \leq \dfrac{d_c}{\beta^j(\underline{x},t)} \\ \mu_d, & \left|\underline{u}_s^j(\underline{x},t)\right| > \dfrac{d_c}{\beta^j(\underline{x},t)} \end{cases}, \quad \underline{x}\in\partial f, j = +,- \tag{28}$$

Here $\alpha_f(\underline{x},t)$ is simplifying notations reading:

$$\alpha_f^j(\underline{x},t)=\frac{1}{2d_c}\left(1-\frac{\mu_d}{\mu_s}\right)\beta^j(\underline{x},t),\quad j=+,- \tag{29}$$

It is worth noting that equations (26)–(29) guarantee $\mu_f(\underline{x},t)=\mu_f^-(\underline{x},t)=\mu_f^+(\underline{x},t)$, and therefore, the traction continuity condition (equation (19)) is ensured.

2.5. Boundary and Initial Conditions

We refer the readers to Jin and Zoback (2017) for details on boundary and initial conditions of the subproblem in the quasi-static regime (section 2.3.1). Here we focus on the subproblem in the dynamic regime only (section 2.3.3). Irrespective of how the fluid effect is resolved, the same boundary and initial conditions are prescribed. First, one can opt for various nonreflecting boundary conditions (Givoli, 1991) for minimizing spurious reflections on $\partial\Omega$. In this study, we implement the classical Lysmer absorbing boundary condition (Lysmer & Kuhlemeyer, 1969) adapted to our model:

$$\begin{cases}\boldsymbol{\sigma}_s(\underline{x},t):\underline{n}\otimes\underline{n}=-a_P\overline{\rho}_{\text{mix}}(t*)\overline{V}_P(t*)\underline{\dot{u}}_s(\underline{x},t)\cdot\underline{n}\\ \boldsymbol{\sigma}_s(\underline{x},t):\underline{n}\otimes\underline{\tau}=-a_S\overline{\rho}_{\text{mix}}(t*)\overline{V}_S(t*)\underline{\dot{u}}_s(\underline{x},t)\cdot\underline{\tau}\end{cases}\quad\forall\underline{x}\in\partial\Omega \tag{30}$$

where a_P and a_S are two dimensionless parameters specifying the degree of absorption (0 and 1 correspond to no absorption and maximum absorption, respectively), $\overline{\rho}_{\text{mix}}(t^*)$ is the spatially averaged fluid density evaluated at t^* by taking the mean of equation (12), and $\overline{V}_p(t^*)$ and $\overline{V}_s(t^*)$ are the average P and S wave velocities of the fluid-saturated solid and are calculated using $\overline{\rho}_{\text{mix}}(t^*)$ and the undrained mechanical parameters shown in equation (11) following standard relations.

Equation (30) states that, on the external boundary, the normal and shear traction scales linearly with the normal and tangential particle velocities by a respective scaling parameter, $-\overline{V}_p(t^*)$ and $-\overline{V}_s(t^*)$. Therefore, equation (30) provides complete energy absorption of waves only at normal incident angles and nonperfect absorption otherwise. To facilitate the variational form as will be shown later, we rewrite equation (30) in the following form:

$$\boldsymbol{\sigma}_s(\underline{x},t)\cdot\underline{n}=-\underline{t}_a(\underline{x},t)\qquad\forall\underline{x}\in\partial\Omega \tag{31}$$

Here for a 2-D problem with boundaries either parallel or perpendicular to the axes

$$\underline{t}_a(\underline{x},t)=\begin{cases}\overline{\rho}_{mix}(t^*)\begin{bmatrix}a_P\overline{V}_P(t^*)\underline{\dot{u}}_s(\underline{x},t)\cdot\underline{e}_1\\ a_s\overline{V}_S(t^*)\underline{\dot{u}}_s(\underline{x},t)\cdot\underline{e}_2\end{bmatrix},\ if\quad\underline{n}\|\underline{e}_1\\ \overline{\rho}_{mix}(t^*)\begin{bmatrix}a_s\overline{V}_S(t^*)\underline{\dot{u}}_s(\underline{x},t)\cdot\underline{e}_1\\ a_P\overline{V}_P(t^*)\underline{\dot{u}}_s(\underline{x},t)\cdot\underline{e}_2\end{bmatrix},\ if\quad\underline{n}\perp\underline{e}_1\end{cases} \tag{32}$$

where $\underline{e}_i(i=1,2)$ is the unit vector along the ith axis.

Second, since we only solve for slip-induced changes in the dynamic subproblem, the initial conditions are trivial to set up. We have, for the displacement and the particle velocity,

$$\underline{u}_s(\underline{x},t^*)=\underline{0}\quad\forall\underline{x}\in\Omega\backslash\partial\Omega \tag{33}$$

$$\underline{\dot{u}}_s(\underline{x},t^*)=\underline{0}\quad\forall\underline{x}\in\Omega\backslash\partial\Omega \tag{34}$$

and for the normal traction on the fault and its rate of change

$$\underline{t}_s(\underline{x},t^*)=\underline{0}\qquad\forall\underline{x}\in\partial f \tag{35}$$

$$\underline{\dot{t}}_s(\underline{x},t^*)=\underline{0}\qquad\forall\underline{x}\in\partial f \tag{36}$$

We note that equation (35) is needed for closing the initial boundary value problem only if the contact condition given by (16) is to be imposed exactly, in which case the fault traction vector becomes an

additional degree of freedom. Noticing equations (20), (22), and (23), we further reduce equations (35) and (36) to the following initial conditions for the contact pressure only and its rate of change. They read

$$t_{sn}(\underline{x}, t^*) = \underline{t}_s(\underline{x}, t^*)\cdot\underline{n}_f = 0 \qquad \forall \underline{x}\in\partial f \tag{37}$$

$$\dot{t}_{sn}(\underline{x}, t^*) = 0 \qquad \forall \underline{x}\in\partial f \tag{38}$$

3. Numerical Formulation: The Subproblem in the Dynamic Regime

We again refer the readers to Jin and Zoback (2017) for details on the variational forms and discretization of the coupled governing equations, specifically, equations (1) and (2), of the quasi-static subproblem (section 2.3.1). There, they assumed transversal uniformity in the fluid velocity within the fault and proposed a hybrid-dimensional two-field mixed finite element method for efficient space discretization and interpolation; a fully implicit Euler scheme was also employed for time discretization. Here we restrict our focus on the coseismic dynamic rupture subproblems (section 2.3.3) and present in particular the numerical formulation of equation (10). For brevity, we omit writing $(\underline{x}, t)$ following space- and time-dependent quantities in this section.

3.1. Variational Form

Let $\underline{\eta}$ be a kinematically admissible variation defined on $\left\{\underline{\eta} : \Omega\rightarrow\mathbb{R}^2 | \underline{\eta}\in\mathbf{H}^1, \underline{\eta} = \underline{0}\ on\ \partial\Omega_u\right\}$, where $\mathbf{H}^1$ denotes a Sobolev space of order 1. $\underline{\eta}$ constitutes the virtual counterpart of the displacement and is permitted to be discontinuous across the fault. Following a standard procedure (e.g., Borja, 2013; Hughes, 2012), we first multiply equation (10) with $\underline{\eta}$ and integrate over the domain volume and then apply integral by parts and subsequently the divergence theorem to push the volume integral onto the domain external boundary as well the two fault surfaces. Exploring the symmetry of the slip-induced stress tensor, noticing the traction continuity condition equation (17), and absorbing boundary condition equation (31), we arrive at the following variational form of equation (10), which reads

$$\iint_\Omega \underline{\eta}\cdot\rho_{\text{mix}}(t*)\ddot{\underline{u}}_s \mathrm{d}\Omega + \int_{\partial\Omega}\underline{\eta}\cdot\underline{t}_a \mathrm{d}\tau + \iint_\Omega \nabla^s\underline{\eta} : \boldsymbol{\sigma}_s \mathrm{d}\Omega + g_c = 0 \tag{39}$$

Here the contact integral reads:

$$g_c = -\left(\int_{\partial f}\underline{\eta}^+\cdot\underline{t}_s^+ \mathrm{d}\tau + \int_{\partial f}\underline{\eta}^-\cdot\underline{t}_s^- \mathrm{d}\tau\right) = \int_{\partial f}[\![\underline{\eta}]\!]\cdot\underline{t}_s \mathrm{d}\tau \tag{40}$$

where $[\![\underline{\eta}]\!] :\ = \underline{\eta}^+ - \underline{\eta}^-$ is the jump of the variation (i.e., the virtual slip) across the fault.

Substituting in equation (20) and then equations (22), (23) into equation (40), the contact integral becomes the following with pore pressure effect and poroelastic effect:

$$g_c = \begin{cases} \int_{\partial f}[\![\underline{\eta}]\!]\cdot[t_{sn}\underline{n}_f + (\mu_f(|\underline{u}_s|))(t_{0n} - p_f(t*) + t_{sn}) - t_{0\tau})\underline{\tau}_s] \mathrm{d}\tau, \text{pore pressure effect} \\ \int_{\partial f}[\![\underline{\eta}]\!]\cdot\left[t_{sn}\underline{n}_f + \left(\mu_f(|\underline{u}_s|)\right)\left(t_{0n} + t_{pn}(t*) + t_{sn}\right) - \left(t_{0\tau} + t_{p\tau}(t*)\right)\right)\underline{\tau}_s] \mathrm{d}\tau, \text{poroelastic effect} \end{cases} \tag{41}$$

The contact constraint (equation (16)) is typically imposed approximately via the penalty method in most earthquake rupture models (e.g., Duan & Oglesby, 2006; Ferronato et al., 2008; Kozdon et al., 2013). This method has the great advantage of unchanged number of degrees of freedom. However, aside from an inexact constraint, that is, the two fault surfaces interpenetrate, the selection of a typically exceedingly large penalty parameter is somewhat arbitrary and requires a trail-and-error process. In this study, we seek to impose the contact constraint exactly and rewrite equation (16) as the following weighted integral form:

$$\int_{\partial f}\varphi[\![\underline{u}_s]\!]\cdot\underline{n}_f \mathrm{d}\tau = 0 \tag{42}$$

where φ is an arbitrary scalar quantity, which can be regarded as the virtual counterpart of the normal traction or the virtual contact pressure.

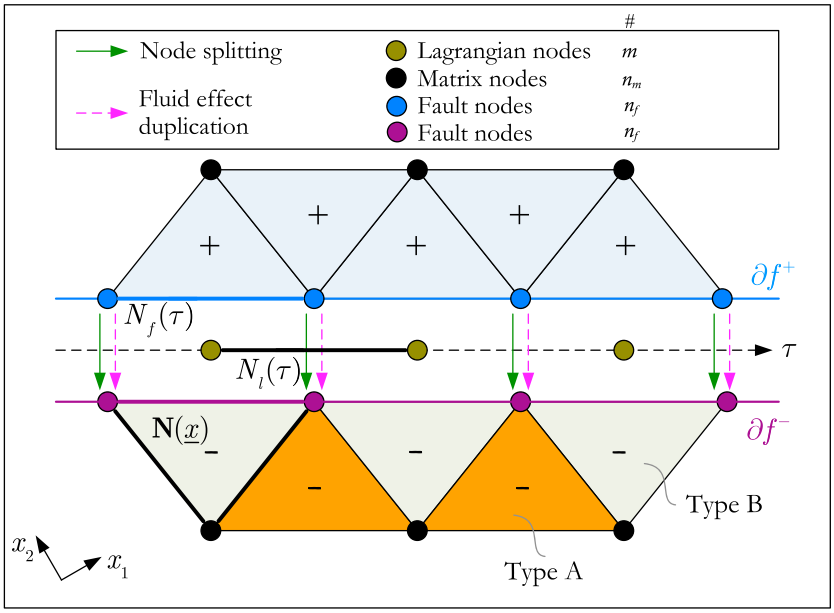

Figure 3. Schematic illustration of mesh processing for the dynamic rupture subproblem. Upon the initiation of fault rupture, fault nodes are split as nodal pairs located on the positive and negative side, respectively. Each pair of nodes have the same coordinates as the original fault node (the two fault surfaces are in contact, and the gap between them is for illustration purposes only). The nodes on the positive side retain the original global nodal indices, while the nodes on the negative side are assigned global nodal indices as $n_m + n_f + 1$, $n_m + n_f + 2$, …, $n_m + n_f + n_f$, where n_m and n_f are the number of the matrix node and the fault node, respectively, before node splitting. Correspondingly, in a standard finite element mesh data structure, the original nodes are supplemented with the newly created nodes, and all elements in contact with the negative side of the fault are updated with the newly assigned node indices. Specifically, type A and type B elements have one and two nodes to be updated, respectively. Upon node splitting, the fluid effect on each fault node is duplicated. Meanwhile, a discrete space consist of a certain number of evenly spaced nodes is generated for interpolating the Lagrangian multiplier (i.e., fault normal traction and contact pressure). The choice of this discrete space can be made by satisfying the LBB condition (section 5). Three elements, including a 2-D matrix element, a 1-D fracture element, and a 1-D element in the Lagrangian space, are highlighted with thickened boarders and lines, and the associated interpolation functions are shown.

3.2. Semidiscrete Form

3.2.1. Space Discretization, Mesh Processing, and Interpolation

The domain is discretized into a set of linear triangular elements perfectly conforming to the predefined fault. For the quasi-static subproblem (section 2.3.1), a single layer of fault nodes is used, whereas for the dynamic subproblem (section 2.3.3), a triple layer of fault nodes is used. Figure 3 illustrates some details of the mesh processing.

We choose $\underline{u}_s$ and t_{sn} as the primary unknowns for this study. The former is interpolated in 2-D using the nodes throughout the domain, whereas the latter is interpolated in 1-D using only the Lagrangian nodes on the fault, see Figure 3. The details are

$$\underline{\eta} \approx \mathbf{N}\underline{c} \tag{43}$$

$$[\![\underline{\eta}]\!] \approx [\![\mathbf{N}]\!]\underline{c} \tag{44}$$

$$\underline{u}_s \approx \mathbf{N}\underline{d} \tag{45}$$

$$[\![\underline{u}_s]\!] \approx [\![\mathbf{N}]\!]\underline{d} \tag{46}$$

$$t_{sn} \approx \underline{N}_l \widehat{l} \tag{47}$$

$$\varphi \approx \underline{N}_l \widehat{\zeta} \tag{48}$$

where $\mathbf{N}$ and $\underline{N}_l$ are the interpolation functions in the discrete 2-D space and the discrete 1-D Lagrangian space, respectively, $\underline{d}$ is the nodal displacement, $\widehat{l}$ is the nodal contact pressure (i.e., the Lagrangian

multiplier), both $\underline{d}$ and $\widehat{l}$ are slip-induced quantities, and $\underline{c}$ and $\widehat{\varsigma}$ are two arbitrary vectors. The forms of the interpolation functions and relevant nodal vectors are given in section A1. Notice in equation (45), a typically present term, $\mathbf{N}_g\underline{d}_g$, arising from the Galerkin approximation is absent here due to the use of the absorbing boundary condition that renders the Dirichelet boundary null (see also Figure 1 caption).

3.2.2. System of Equations

Substituting equations (43)–(48) into equations (39) and (42), canceling $\underline{c}$ and $\widehat{\varsigma}$, noticing equation (41), and following a Voigt notation, we arrive at the following semidiscrete form of the equation written in a matrix form (excluding the $\mathbf{C}^{\mathbf{R}}$ term) after some rearrangement:

$$\begin{bmatrix} \mathbf{M}_{n\times n} & \mathbf{0}_{n\times m} \\ \mathbf{0}_{m\times n} & \mathbf{0}_{m\times m} \end{bmatrix} \begin{Bmatrix} \ddot{\underline{d}}_{n\times 1} \\ \ddot{\widehat{l}}_{m\times 1} \end{Bmatrix} + \begin{bmatrix} \left(\mathbf{C}^A + \mathbf{C}^R\right)_{n\times n} & \mathbf{0}_{n\times m} \\ \mathbf{0}_{m\times n} & \mathbf{0}_{m\times m} \end{bmatrix} \begin{Bmatrix} \dot{\underline{d}}_{n\times 1} \\ \dot{\widehat{l}}_{m\times 1} \end{Bmatrix} + \begin{bmatrix} \mathbf{K}_{n\times n} & \mathbf{G}_{n\times m} \\ \mathbf{G}^T{}_{m\times n} & \mathbf{0}_{m\times m} \end{bmatrix} \begin{Bmatrix} \underline{d}_{n\times 1} \\ \widehat{l}_{m\times 1} \end{Bmatrix} = \begin{Bmatrix} \underline{F}_{n\times 1}\left(\underline{d}, \widehat{l}\right) \\ \widehat{0}_{m\times 1} \end{Bmatrix} \tag{49}$$

where $\mathbf{M}$ and $\mathbf{K}$ are the mass matrix and the elastic stiffness matrix of the faulted system (they differ from those of a fault-free system), $\mathbf{C}^A$ is an equivalent damping matrix arising from the prescription of an absorbing boundary condition, $\mathbf{G}$ is the contact matrix, and $\underline{F}$ is an equivalent external nodal force driving/resisting the rupture. The sizes of $\underline{d}$ and $\widehat{l}$ are indicated as n and m, respectively. Here m is the number of the Lagrangian nodes, and $n = (n_m + n_f \times 2) \times 2$, see Figure 3.

Here

$$\mathbf{M} = \iint_\Omega \mathbf{N}^T \rho_{\text{mix}}(t*)\mathbf{N}\mathrm{d}\Omega \tag{50}$$

$$\mathbf{C}^A = \int_{\partial\Omega} \mathbf{N}^T \overline{\rho}_{\text{mix}}(t*)\mathbf{V}^{(\partial\Omega)}\mathbf{N}\mathrm{d}\tau \tag{51}$$

$$\mathbf{K} = \iint_\Omega \mathbf{B}^T \mathbb{C}_u \mathbf{B}\mathrm{d}\Omega \tag{52}$$

$$\mathbf{G} = \int_{\partial f} [\![\mathbf{N}]\!]^T \underline{n}_f \underline{N}_l \mathrm{d}\tau \tag{53}$$

$$\underline{F}\left(\underline{d}, \widehat{l}\right) = \begin{cases} \int_{\partial f} [\![\mathbf{N}]\!]^T \underline{\tau}_s \left[t_{0\tau} - \mu_f\left(|\underline{d}|\right)\left(t_{0n} - p_f(t*) + \underline{N}_l \widehat{l}\right)\right]\mathrm{d}\tau, \text{pore pressure effect} \\ \int_{\partial f} [\![\mathbf{N}]\!]^T \underline{\tau}_s \left[\left(t_{0\tau} + t_{p\tau}(t*)\right) - \mu_f\left(|\underline{d}|\right)\left(t_{0n} + t_{pn}(t*) + \underline{N}_l \widehat{l}\right)\right]\mathrm{d}\tau, \text{poroelastic effect} \end{cases} \tag{54}$$

In equation (51), $\mathbf{V}^{(\partial\Omega)}$ is given by the following (here we give the elementwise expression):

$$\mathbf{V}^{(\partial\Omega)} = \begin{cases} \begin{bmatrix} a_p \overline{V}_P(t^*) & \\ & a_s \overline{V}_S(t^*) \end{bmatrix}, \text{if} \quad \partial\Omega \perp \underline{e}_1 \left(\underline{n} \parallel \underline{e}_1\right) \\ \begin{bmatrix} a_s \overline{V}_S(t^*) & \\ & a_p \overline{V}_P(t^*) \end{bmatrix}, \text{if} \quad \partial\Omega \parallel \underline{e}_1 \left(\underline{n} \perp \underline{e}_1\right) \end{cases} \tag{55}$$

In equation (52), $\mathbf{B}$ is the displacement-strain transformation matrix, and $\mathbb{C}_u$ is the undrained elastic stiffness matrix of the fluid-saturated solid under plane strain. The expressions of $\mathbf{B}$, $\mathbb{C}_u$, and the other finite element discretization matrices are given in section A1.

Equation (54) is obtained by moving the component related to the slip-induced shear traction in the contact integral g_c (see equation (51)) to the right hand side, leading to the symmetric structure of equation (49). As can be seen from equation (54), the consideration of frictional sliding and therefore the associated consistency condition (equations (22) and (23)) render equation (49) nonlinear with respect to the nodal values of the contact pressure, $\widehat{l}$; further, because of the dynamically evolving frictional strength of the fault (equation (24)), equation (49) is also nonlinear with respect to the nodal values of the slip-induced displacement, $\underline{d}$. For the coseismic dynamic rupture, the formulations show that the fluid effect enters not the mass,

damping, or stiffness matrices of the system but only the equivalent external nodal force, albeit in different manners when being resolved as pore pressure effect or poroelastic effect.

Finally, $\mathbf{C^R}$ in equation (49) is an artificially introduced viscous damping matrix to suppress spurious oscillations of high frequencies. Here we employ the classical mass- and stiffness- proportionate damping matrix, known as the Rayleigh damper (see, e.g., Duan & Oglesby, 2006; Liu & Gorman, 1995), which reads

$$\mathbf{C}^R = a\mathbf{M} + b\mathbf{K} \tag{56}$$

where a and b are the Rayleigh damping coefficients.

Solving equation (49) gives the nodal displacement, along with the nodal particle velocity and acceleration. The stress at each time step can be calculated according to

$$\boldsymbol{\sigma}_s = \mathbb{C}_u \mathbf{B} \underline{d} \tag{57}$$

3.3. Fully Discrete Form

The solution to equation (49) is advanced in time using a finite difference discretization method. Most earthquake rupture models opt for an explicit time stepping scheme (e.g., Aagaard et al., 2013; Duan & Oglesby, 2006; de la Puente et al., 2009), therefore are subjected to the well-known Courant-Friedrichs-Lewy (CFL) constraint (Courant et al., 1928). Here we opt for the following implicit method from the Newmark family (Newmark, 1959), which offers unconditional stability and second-order accuracy, to discretize equation (49) in time. Denoting $\dot{\underline{d}}, \dot{\widehat{l}}$ as $\underline{v}_d, \widehat{v}_l$, and $\ddot{\underline{d}}, \ddot{\widehat{l}}$ as $\underline{a}_d, \widehat{a}_l$, the discretization procedure is composed of the following three steps. First, predict the displacement and the particle velocity together with the contact pressure and its speed of change:

$$\begin{aligned}
\begin{pmatrix} \widetilde{\underline{v}}_d \\ \widetilde{\widehat{v}}_l \end{pmatrix}^{(n+1)} &= \begin{pmatrix} \underline{v}_d \\ \widehat{v}_l \end{pmatrix}^{(n)} + \frac{1}{2}\delta t \begin{pmatrix} \underline{a}_d \\ \widehat{a}_l \end{pmatrix}^{(n)} \\
\begin{pmatrix} \widetilde{\underline{d}} \\ \widetilde{\widehat{l}} \end{pmatrix}^{(n+1)} &= \begin{pmatrix} \underline{d} \\ \widehat{l} \end{pmatrix}^{(n)} + \delta t \begin{pmatrix} \underline{v}_d \\ \widehat{v}_l \end{pmatrix}^{(n)} + \frac{1}{4}\delta t^2 \begin{pmatrix} \underline{a}_d \\ \widehat{a}_l \end{pmatrix}^{(n)}
\end{aligned} \tag{58}$$

Second, solve the following nonlinear equation of a saddle-point structure for the updated particle acceleration together with the updated acceleration of change in the contact pressure:

$$\begin{aligned}
&\left(\begin{bmatrix} \mathbf{M} & \mathbf{0} \\ \mathbf{0} & \mathbf{0} \end{bmatrix} + \frac{1}{2}\delta t \begin{bmatrix} \mathbf{C}^A + \mathbf{C}^R & \mathbf{0} \\ \mathbf{0} & \mathbf{0} \end{bmatrix} + \frac{1}{4}\delta t^2 \begin{bmatrix} \mathbf{K} & \mathbf{G} \\ \mathbf{G}^T & \mathbf{0} \end{bmatrix} \right) \begin{pmatrix} \underline{a}_d \\ \widehat{a}_l \end{pmatrix}^{(n+1)} \\
&= \left(\begin{pmatrix} \underline{F} \\ \widehat{0} \end{pmatrix}^{(n+1)} - \begin{bmatrix} \mathbf{C}^A + \mathbf{C}^R & \mathbf{0} \\ \mathbf{0} & \mathbf{0} \end{bmatrix} \begin{pmatrix} \widetilde{\underline{v}}_d \\ \widetilde{\widehat{v}}_l \end{pmatrix}^{(n+1)} - \begin{bmatrix} \mathbf{K} & \mathbf{G} \\ \mathbf{G}^T & \mathbf{0} \end{bmatrix} \begin{pmatrix} \widetilde{\underline{d}} \\ \widetilde{\widehat{l}} \end{pmatrix}^{(n+1)} \right)
\end{aligned} \tag{59}$$

And third, update the particle velocity and the displacement together with the contact pressure and its speed of change:

$$\begin{aligned}
\begin{pmatrix} \underline{v}_d \\ \widehat{v}_l \end{pmatrix}^{(n+1)} &= \begin{pmatrix} \widetilde{\underline{v}}_d \\ \widetilde{\widehat{v}}_l \end{pmatrix}^{(n+1)} + \frac{1}{2}\delta t \begin{pmatrix} \underline{a}_d \\ \widehat{a}_l \end{pmatrix}^{(n+1)} \\
\begin{pmatrix} \underline{d} \\ \widehat{l} \end{pmatrix}^{(n+1)} &= \begin{pmatrix} \widetilde{\underline{d}} \\ \widetilde{\widehat{l}} \end{pmatrix}^{(n+1)} + \frac{1}{4}\delta t^2 \begin{pmatrix} \underline{a}_d \\ \widehat{a}_l \end{pmatrix}^{(n+1)}
\end{aligned} \tag{60}$$

In equations (58)–(60), δt is the time increment, subscripts (n) and $(n+1)$ indicate the current and the next time steps, respectively, and the cap "~" indicates intermediate predictions.

4. Linearization: The Subproblem in the Dynamic Regime

The detailed linearization procedure of the quasi-static subproblem is given in Jin and Zoback (2017). Here we focus on the dynamic subproblem only. The key step lies in solving equation (59) that is nonlinear. Here we implement the classic Newton-Raphson linearization scheme, which reads

$$\mathbf{J}\left(\underline{\varsigma}^{(n+1,k)},\mathrm{d}t\right)\left(\underline{\varsigma}^{(n+1,k+1)}-\underline{\varsigma}^{(n+1,k)}\right)=-\underline{R}\left(\underline{\varsigma}^{(n+1,k)},\underline{\varsigma}^{(n)},\mathrm{d}t\right) \tag{61}$$

where $\mathbf{J}$ is the Jacobian matrix, $\underline{R}$ is the residual vector, $\underline{\varsigma}=(\underline{a}_d,\widehat{a}_l)^T$ is the collectively written unknown vector, and subscripts (k) and ($k+1$) indicates two successive Newton iteration steps.

The residual vector, which varies between the decoupled and coupled approaches, reads the following:

$$\begin{aligned}\underline{R}^{(n+1,k)}&=\begin{pmatrix}\underline{R}_d^{(n+1,k)}\\ \underline{R}_l^{(n+1,k)}\end{pmatrix}=\begin{pmatrix}\mathbf{M}+\frac{1}{2}\delta t\left(\mathbf{C}^A+\mathbf{C}^R\right)+\frac{1}{4}\delta t^2\mathbf{K} & \frac{1}{4}\delta t^2\mathbf{G}\\ \frac{1}{4}\delta t^2\mathbf{G}^T & \mathbf{0}\end{pmatrix}^{(n+1,k)}\begin{pmatrix}\underline{a}_d\\ \widehat{a}_l\end{pmatrix}\\ &-\left[\begin{pmatrix}\underline{F}\left(\underline{d}^{(n+1,k)},\widehat{l}^{(n+1,k)}\right)\\ \widehat{0}\end{pmatrix}-\begin{pmatrix}\mathbf{C}^A+\mathbf{C}^R & \mathbf{0}\\ \mathbf{0} & \mathbf{0}\end{pmatrix}\begin{pmatrix}\widetilde{v}_d\\ \widetilde{\widehat{v}}_l\end{pmatrix}^{(n+1)}-\begin{pmatrix}\mathbf{K} & \mathbf{G}\\ \mathbf{G}^T & \mathbf{0}\end{pmatrix}\begin{pmatrix}\widetilde{d}\\ \widetilde{\widehat{l}}\end{pmatrix}^{(n+1)}\right]\approx\underline{0}\end{aligned} \tag{62}$$

where $\underline{F}\left(\underline{d}^{(n+1,k)},\widehat{l}^{(n+1,k)}\right)$ is the equivalent external nodal force vector evaluated at time step ($n+1$) and Newton iteration step (k) and is obtained by substituting $\underline{d}^{(n+1,k)}$ and $\widehat{l}^{(n+1,k)}$ into equation (54), leading to

$$\begin{aligned}&\underline{F}\left(\underline{d}^{(n+1,k)},\widehat{l}^{(n+1,k)}\right)\\ &=\begin{cases}\int_{\partial f}[\![\mathbf{N}]\!]^T\underline{\tau}_s\left[t_{0\tau}-\left(1-2\alpha_f{}^{(n+1,k)}\left|\underline{d}^{(n+1,k)}\right|\right)\mu_s\left(t_{0n}-p_f(t^*)+\underline{N}_l\widehat{l}^{(n+1,k)}\right)\right]\mathrm{d}\tau, & \left|\underline{d}^{(n+1,k)}\right|\le\frac{d_c}{\beta^{(n+1,k)}}\\ \int_{\partial f}[\![\mathbf{N}]\!]^T\underline{\tau}_s\left[t_{0\tau}-\mu_d\left(t_{0n}-p_f(t^*)+\underline{N}_l\widehat{l}^{(n+1,k)}\right)\right]\mathrm{d}\tau, & \left|\underline{d}^{(n+1,k)}\right|>\frac{d_c}{\beta^{(n+1,k)}}\end{cases}\end{aligned} \tag{63}$$

with pore pressure effect and

$$\begin{aligned}&\underline{F}\left(\underline{d}^{(n+1,k)},\widehat{l}^{(n+1,k)}\right)=\\ &\begin{cases}\int_{\partial f}[\![\mathbf{N}]\!]^T\underline{\tau}_s\left[\left(t_{0\tau}+t_{p\tau}(t^*)\right)-\left(1-2\alpha_f{}^{(n+1,k)}\left|\underline{d}^{(n+1,k)}\right|\right)\mu_s\left(t_{0n}+t_{pn}(t^*)+\underline{N}_l\widehat{l}^{(n+1,k)}\right)\right]\mathrm{d}\tau, & \left|\underline{d}^{(n+1,k)}\right|\le\frac{d_c}{\beta^{(n+1,k)}}\\ \int_{\partial f}[\![\mathbf{N}]\!]^T\underline{\tau}_s\left[\left(t_{0\tau}+t_{p\tau}(t^*)\right)-\mu_d\left(t_{0n}+t_{pn}(t^*)+\underline{N}_l\widehat{l}^{(n+1,k)}\right)\right]\mathrm{d}\tau, & \left|\underline{d}^{(n+1,k)}\right|>\frac{d_c}{\beta^{(n+1,k)}}\end{cases}\end{aligned} \tag{64}$$

with poroelastic effect.

In equations (63) and (64), $\beta^{(n+1,k)}$ and $\alpha_f^{(n+1,k)}$ can be computed by substituting $\underline{d}^{(n+1,k)}$ into equations (27) and (29), respectively. The former requires the calculation of $\gamma^{(n+1,k)}$, which can be obtained from $\underline{d}_s^{+,(n+1,k)}$ and $\underline{d}_s^{-,(n+1,k)}$ according to equation (25).

The Jacobian matrix, computed at time step ($n+1$) and Newton iteration step (k), takes the form of

$$\mathbf{J}^{(n+1,k)}=\begin{bmatrix}\mathbf{J}_{11} & \mathbf{J}_{12}\\ \mathbf{J}_{21} & \mathbf{J}_{22}\end{bmatrix}^{(n+1,k)}=\begin{bmatrix}\frac{\partial\underline{R}_d^{(n+1,k)}}{\partial\underline{a}_d^{(n+1,k)}} & \frac{\partial\underline{R}_d^{(n+1,k)}}{\partial\widehat{a}_l^{(n+1,k)}}\\ \frac{\partial\underline{R}_l^{(n+1,k)}}{\partial\underline{a}_d^{(n+1,k)}} & \frac{\partial\underline{R}_l^{(n+1,k)}}{\partial\widehat{a}_l^{(n+1,k)}}\end{bmatrix} \tag{65}$$

Here the four block submatrices are given as

$$\mathbf{J}_{11}{}^{(n+1,k)} = \left(\mathbf{M} + \frac{1}{2}\delta t\left(\mathbf{C}^A + \mathbf{C}^R\right) + \frac{1}{4}\delta t^2\mathbf{K}\right) - \begin{cases} \underbrace{\frac{1}{4}\delta t^2 \int_{\partial f} [\![\mathbf{N}]\!]^T \underline{\tau}_s \left[2\alpha_f{}^{(n+1,k)}\mu_s\left(t_{0n} + f + \underline{N}_l\widehat{l}^{(n+1,k)}\right)\right] \mathrm{d}\tau \cdot \underline{e}_d \mathbf{1}}_{\mathbf{Q}^{(n+1,k)}}, & \left|\underline{d}^{(n+1,k)}\right| \le \frac{d_c}{\beta^{(n+1,k)}} \\ \mathbf{0}, & \left|\underline{d}^{(n+1,k)}\right| > \frac{d_c}{\beta^{(n+1,k)}} \end{cases} \tag{66}$$

$$\mathbf{J}_{12}{}^{(n+1,k)} = \frac{1}{4}\delta t^2\mathbf{G} - \begin{cases} \frac{1}{4}\delta t^2 \int_{\partial f} [\![\mathbf{N}]\!]^T \underline{\tau}_s \left[-\left(1 - 2\alpha_f{}^{(n+1,k)}\left|\underline{d}^{(n+1,k)}\right|\right)\mu_s \underline{N}_l\right] \mathrm{d}\tau \mathbf{1}, & \left|\underline{d}^{(n+1,k)}\right| \le \frac{d_c}{\beta^{(n+1,k)}} \\ \frac{1}{4}\delta t^2 \int_{\partial f} [\![\mathbf{N}]\!]^T \underline{\tau}_s [-\mu_d \underline{N}_l] \mathrm{d}\tau \mathbf{1}, & \left|\underline{d}^{(n+1,k)}\right| > \frac{d_c}{\beta^{(n+1,k)}} \end{cases} \tag{67}$$

$$\mathbf{J}_{21}{}^{(n+1,k)} = \mathbf{J}_{21} = \frac{1}{4}\delta t^2\mathbf{G}^T \tag{68}$$

$$\mathbf{J}_{22}{}^{(n+1,k)} = \mathbf{J}_{22} = \mathbf{0} \tag{69}$$

In equations (66) and (67), $\mathbf{1}$ is the unit identity with size equal to the size of $\mathbf{J}_{11}$and $\mathbf{J}_{12}$, respectively, $\underline{e}_d$ is a vector containing unit subvectors specifying the direction of the nodal displacements, and $\mathbf{Q}$ is defined for later use (section 6.2). The expression of $\underline{e}_d$ and some other intermediate expressions for arriving at the final Jacobian matrix are provided in section A2. Notice that the Jacobian matrix, which is asymmetric, is almost identical for the two approaches except for the block submatrix $\mathbf{J}_{11}$ in which the f reads

$$f = \begin{cases} -p_f(t^*), & \text{pore pressure effect} \\ t_{pn}(t^*), & \text{poroelastic effect} \end{cases} \tag{70}$$

Within each time step, the Newton iteration is terminated when the following criteria, where $\mathrm{tol}_{\mathrm{NR}}$ is a predefined tolerance, are met:

$$\left\|\underline{R}\left(\underline{\varsigma}^{(n+1,k+1)}\right)\right\|_2 \le \mathrm{tol}_{\mathrm{NR}}, \quad \left\|\underline{a}_d{}^{(n+1,k+1)} - \underline{a}_d{}^{(n+1,k)}\right\|_2 \le 0.01\left\|\underline{a}_d{}^{(n)}\right\|_2, \quad \left\|\widehat{a}_l{}^{(n+1,k+1)} - \widehat{a}_l{}^{(n+1,k)}\right\|_2 \le 0.01\left\|\widehat{a}_l{}^{(n)}\right\|_2 \tag{71}$$

5. Stabilization of Contact Pressure

Depending on the discretization scheme and the way of imposing the contact constraint, the semidiscrete form and, subsequently, the fully discrete form of the contact problem sometimes become a conical saddle point system. It typically arises from the following two combinations: (1) a standard dual finite element discretization scheme that is suitable for nongrowing contact surfaces, combined with the Lagrangian multiplier method that imposes the contact condition exactly, and (2) an extended finite element discretization scheme that can handle randomly propagating contact surface without remeshing, combined with either the Lagrangian multiplier method or the Penalty method, the latter imposing the contact condition approximately. The first combination results in a mixed-dimensional interpolation where the displacement and the contact pressure are interpolated in n-D and (n-1)-D, respectively, whereas the second combination leads to an equal-dimensional interpolation of both unknowns. Here our formulation falls within the first category, and the semidiscrete form equation (49) as well as the fully discrete form equation (59) are of a saddle point structure. The second category can be found in Liu & Borja (2010).

Irrespective of the combination of choice, the well-known Ladyženskaja-Babuška-Brezzi (LBB) compatibility condition (Babuška, 1973; Brezzi, 1974; Brezzi & Bathe, 1990; Ladyzhenskaya, 1969), also broadly referred to as the so-called discrete inf-sup condition, is necessary and sufficient for the well posedness of such problems. Satisfaction of the LBB condition requires careful selection of the discrete space and the associated

interpolation schemes for the primal variable (the contact pressure) and the dual variable (the displacement). For example, in the case of the second combination, the problem resembles that resulted from a mixed finite element discretization of a coupled poromechanical problem, therefore, one can opt for the classical Tylor-Hood family of stabilized finite element, in which the interpolation of the displacement is 1 order higher than that of the normal contact pressure, leading to an equal-dimensional mixed-order interpolation scheme. Unfortunately, the seemingly intuitive equal-low-order interpolation pair violates the LBB condition; consequently, pronounced numerical instability occurs in the form of spurious oscillation in the contact pressure. To overcome this drawback, some stabilization techniques have been developed, typically through modifying the variational form of the contact constraint (equation (42)) and replacing the zero block submatrix (equation (69)) with a nonzero block matrix in order to satisfy a *weaker* LBB condition (Béchet et al., 2009; Liu & Borja, 2010). In a similar manner, this strategy is equally applicable to the coupled poromechanical problem of a single-porosity system (White & Borja, 2008) and a dual-porosity system (Choo & Borja, 2015). In a sense, the nonphysical oscillation in the (contact, fluid) pressure is numerically smeared to obtain a meaningfully smoothed solution. It is perhaps less trivial to be applied to the first set of combination as the interpolation is mixed dimensional. Hence, in our case, utilization of a stable Lagrangian space is essential.

The construction of a stable Lagrangian space is dependent on the discretization of the two surfaces of the discontinuity, including a node-on-surface discretization and a node-on-node discretization. In either case, it seems convenient and only logical to let the number of Lagrangian multipliers be identical to the number of nodes on either fault surface. However, it has been shown that in the case of node-on-surface discretization, such a choice, in general and irrespective of the order of interpolation, violates the LBB condition for a two deformable body contact problem (Solberg & Papadopoulos, 2005). Refining the discrete space for Lagrangian multipliers will exacerbate rather than suppress the oscillation. In contrast, utilizing a uniformly distributed subset of the fault nodes and, therefore, a reduced number of Lagrangian multipliers allows stability (and even passing the patch test to eliminate surface locking) even in the case of low-order interpolations of both field variables. In other words, to guarantee stability, the ratio of the number of fault nodes on either fault surface to the number of Lagrangian multipliers should be above 1, and the optimal ratio is shown to be 2. One obvious choice is then to let the nodes for Lagrangian multipliers coincide with every two fault nodes on either contact surface and utilize linear interpolation. This requires the fault to be discretized into an even number of segments (n_f is an odd number, see Figure 3), and the ratio is $2n_f/(n_f+1) \approx 2$, providing a near optimal ratio. This approach involves more complicated integration procedures when calculating equation (53). An alternative, as is adopted in this study, is to use a node-to-node discrete space on the two fault surfaces as naturally obtained from node splitting, together with a coincident discrete space for Lagrangian multipliers, such that $m = n_f$, and that for any point on the fault

$$\underline{N}_l(\tau) \equiv \underline{N}_f(\tau) \tag{72}$$

This approach satisfies the LBB condition as well as passes the patch test (El-Abbasi & Bathe, 2001).

6. Iterative Solver and Preconditioner

6.1. Iterative Solver Selection

Upon assembly of the relevant matrices and vectors shown in equations (50)–(54), the major computational cost then arises from solving equation (61), which needs to be carried out for each time step shown by equation (59). In theory, the solution can be written in the form of $\underline{\varsigma}^{(n+1,k+1)} = \underline{\varsigma}^{(n+1,k)} + \mathbf{J}^{-1}(-\underline{R})$, but the sparse nature of the Jacobian $\mathbf{J}$ typically precludes a direct computation of $\mathbf{J}^{-1}$. Instead, an iterative type of solver, typically from the nonstationary family of linear solvers, is required for memory efficiency and, more importantly, better accuracy in the solution. The selection of a suitable Krylov subspace iterative solver is dependent on the symmetry and positive definiteness of $\mathbf{J}$, see, for example, Wathen (2015) for comprehensive review. To this aim, we briefly underscore two specific points pertaining to our formulation. First, unlike the penalty method, the contact condition is imposed exactly via the Lagrangian multiplier method. This leads to a saddle point structure (also referred to as a KKT structure in optimization theories) of $\mathbf{J}$ in which $\mathbf{J}_{22}$ is a zero-constituent matrix. $\mathbf{J}$ is therefore indefinite, usually precluding the use of some most popular solvers like the conjugate gradient solver that requires the coefficient matrix to be symmetric and positive definite. Under simplified conditions, specifically, if the sliding is frictionless, then the problem is linear with a

symmetric coefficient matrix and can be solved by paring the conjugate gradient solver with some symmetric indefinite preconditioners, also referred to as the *constraint preconditioners* (e.g., Benzi & Wathen, 2008; Schöberl & Zulehner, 2007). Such an approach is adopted in some rupture code like FaultMod (Barall, 2009). Second, when accounting for friction, **J** becomes asymmetric and therefore rendering solvers like minimal residual and symmetric linear quadratic unsuitable, since both are only applicable to a symmetric, albeit, indefinite system. Additionally, the preconditioned **J** (section 6.2) generally becomes asymmetric, even if **J** and the preconditioner themselves are symmetric. We are therefore left with more general solvers like generalized minimal residual method (GMRES) and BiCGStab, both capable of handling an asymmetric and indefinite system. We refer to Barrett et al. (1994) for a comprehensive review as well as the algorithmic details of the aforementioned solvers. In this study, we opt for the GMRES solver over the BiCGStab solver as the former has an orthogonal Krylov subspace basis that provides optimal convergence behaviors (Benzi et al., 2005).

6.2. Preconditioner Design

Irrespective of the way of imposing the contact condition, the coefficient matrix arising from a contact problem is typically severely ill conditioned. Therefore, a preconditioner is required to accelerate (or even just allow for) convergence of the iterative solver. For example, Ferronato et al. (2008) designed a mixed constraint preconditioner for a canonical symmetric positive definite but ill-conditioned coefficient matrix arising from imposing the contact condition inexactly via the penalty approach. In our case, **J** is severely ill conditioned, due to first its saddle point structure, and, second, the radical *contrast*, among, for example, the L_2 norm, of the constituent submatrices, depending specifically on the size of the finite elements as well as the given material properties. Therefore, the system described by equation (59) needs to be preconditioned to gain better spectral properties favoring the convergence of our selected solver. We refer to Benzi et al. (2005) for a comprehensive review on preconditioners for saddle point systems. Specific to fault rupture problems, several preconditioners have been proposed and tested on the GMRES solver (Aagaard et al., 2013). These preconditioners are stationary (i.e., they do not vary throughout the problem) and are designed for a symmetric saddle point coefficient matrix for a quasi-static dislocation problem in the absences of fluid. Here we aim to design an efficient, physics-based and dynamically evolving preconditioner for the frictional dynamic rupture problem in the presence of fluid. We begin by constructing several algebraic preconditioners and subpreconditioners based on the entries of the Jacobian. We then test their performances, when paired with the GMRES solver, in solving the saddle point system arising from a frictional rupture problem in which the effect of fault fluid is reflected in the residual vector, before we subsequently determine a most effective preconditioner. Lastly, by drawing similarity between the quasi-static dislocation problem and the dynamic rupture problem at a given time step, both subjected to the same fault fluid effect (i.e., both have the same residual vector), we take the form of the selected preconditioner and customize it to the dynamic rupture problem by including the chosen time step and other matrices associated with the time-dependent terms.

A left-preconditioned saddle point system shown by equation (61) can be written in the following general canonical form:

$$\mathbf{P}^{-1}\underbrace{\begin{bmatrix}\mathbf{A} & \mathbf{B}_1{}^T\\ \mathbf{B}_2 & \mathbf{0}\end{bmatrix}}_{\mathbf{J}}\begin{pmatrix}\underline{y}_1\\ \underline{y}_2\end{pmatrix} = \mathbf{P}^{-1}\begin{pmatrix}\underline{f}\\ \underline{g}\end{pmatrix} \tag{73}$$

where **P** is the (left) preconditioner, and **J** is the Jacobian.

Ideally, $\mathbf{P}^{-1} \approx \mathbf{J}^{-1}$ such that eigenvalues of the preconditioned coefficient matrix $\mathbf{P}^{-1}\mathbf{J}$ are clustered around 1. The first step is then to choose the form of **P** such that it will best allow for this property. This can be achieved by exploring the block structure of **J**, which, when the constituent block matrix **A** is nonsingular, admits the following **LDU** block triangular factorization:

$$\mathbf{J} = \underbrace{\begin{bmatrix}\mathbf{I} & \mathbf{0}\\ \mathbf{B}_2\mathbf{A}^{-1} & \mathbf{I}\end{bmatrix}}_{\mathbf{L}}\underbrace{\begin{bmatrix}\mathbf{A} & \mathbf{0}\\ \mathbf{0} & \mathbf{S}\end{bmatrix}}_{\mathbf{D}}\underbrace{\begin{bmatrix}\mathbf{I} & \mathbf{A}^{-1}\mathbf{B}_1^T\\ \mathbf{0} & \mathbf{I}\end{bmatrix}}_{\mathbf{U}} \tag{74}$$

where **L**, **D**, and **U** are factorized matrices. Here, **S** is the so-called Schur complement of **A** in **J**, which reads

$$\mathbf{S} = -\mathbf{B}_2\mathbf{A}^{-1}\mathbf{B}_1{}^T \tag{75}$$

We also define the following matrix as a variation of the diagonal matrix **D**:

$$\mathbf{D}' = \begin{bmatrix} \mathbf{A} & \mathbf{0} \\ \mathbf{0} & -\mathbf{S} \end{bmatrix} \tag{76}$$

Based on equation (74), several natural choices of **P** can be readily obtained. For example, White et al. (2016) summarized several preconditioners, both left and right, through different combinations of **L**, **D**, and **U**, for a similar saddle point system arising from mixed finite discretization of coupled partial differential equations governing a poromechanical system. The right preconditioner, which is in an upper block-triangular form, has also been tested in the rupture problem (Aagaard et al., 2013). Further, as was summarized in Benzi and Wathen (2008), the use of $\mathbf{D}'$ instead of **D** leads to a diagonalizable preconditioned matrix that allows for excellent convergence behaviors of GMRES. Therefore, in constructing a left preconditioner **P**, we choose a block-diagonal (indefinite) preconditioner:

$$\mathbf{P}_d = \mathbf{D}' \rightarrow \mathbf{P}_d{}^{-1} = \left(\mathbf{D}'\right)^{-1} = \begin{bmatrix} \mathbf{A}^{-1} & \mathbf{0} \\ \mathbf{0} & -\mathbf{S}^{-1} \end{bmatrix} \tag{77}$$

and a lower block-triangular (indefinite) preconditioner:

$$\mathbf{P}_t = \mathbf{L}\mathbf{D}' = \begin{bmatrix} \mathbf{A} & \mathbf{0} \\ \mathbf{B}_2 & -\mathbf{S} \end{bmatrix} \rightarrow \mathbf{P}_t{}^{-1} = \left(\mathbf{D}'\right)^{-1}\mathbf{L}^{-1} = \begin{bmatrix} \mathbf{A}^{-1} & \mathbf{0} \\ \mathbf{S}^{-1}\mathbf{B}_2\mathbf{A} & -\mathbf{S}^{-1} \end{bmatrix} \tag{78}$$

Note that, in the above two equations, the use of $-\mathbf{S}$ instead of **S** could render $\mathbf{P}_t$ indefinite, and its inverse may not exist. Nonetheless, as will be shown shortly, this will not pose any problem in solving the preconditioned system using an iterative solver. As shown by equations (75)– (78), implementation of these two essentially idealized preconditioners requires the inverse $\mathbf{A}^{-1}$ and $\mathbf{S}^{-1}$, which are usually dense and may not be available. While preconditioner based on one-level Schur reduction has shown to be applicable to rupture problems (Aagaard et al., 2013), in practice, it is more economical to use the following subpreconditioner by replacing **A** and **S** with their respective approximations $\widehat{\mathbf{A}}$ and $\widehat{\mathbf{S}}$:

$$\mathbf{P}_j \leftarrow \widehat{\mathbf{P}}_j (j = d, t) \tag{79}$$

Good choice of $\widehat{\mathbf{A}}$ and $\widehat{\mathbf{S}}$ are then central to the overall effectiveness of the preconditioners. Two commonly used approaches for obtaining $\widehat{\mathbf{A}}$ are

$$\widehat{\mathbf{A}} = \text{diag}(\mathbf{A}) \tag{80}$$

and

$$\widehat{\mathbf{A}} = \widehat{\mathbf{L}}\widehat{\mathbf{L}}^T \tag{81}$$

Equation (80) simply takes the diagonal components of **A** to construct $\widehat{\mathbf{A}}$, while equation (81) performs the so-called incomplete Cholesky factorization, the details of which can be found in many standard texts.

The choice of $\widehat{\mathbf{S}}$, on the other hand, is a less trivial task. One can of course circumvent the problem by simply replacing $\widehat{\mathbf{S}}$ with a unit block matrix and reducing $\mathbf{P}_j (j = d, t)$ into a so-called algebraic multigrid preconditioner, as has been tested in rupture problems (Aagaard et al., 2013). An alternative is to choose $\widehat{\mathbf{S}}$ as the mass matrix scaled by an appropriate constant specific to the problem at hand, as has been tested in coupled poromechanical problems (White et al., 2016; White & Borja, 2011). Another approach, as is adopted here, is to retain the form of equation (75) and compute $\widehat{\mathbf{S}}$ using the approximation $\widehat{\mathbf{A}}$. This approach has been demonstrated efficient for coupled poromechanical problems (see, e.g., Castelletto et al., 2016; Ferronato et al., 2010). Here we apply it to the rupture problem. $\widehat{\mathbf{S}}$ thus reads

$$\widehat{\mathbf{S}} = -\mathbf{B}_2\widehat{\mathbf{A}}^{-1}\mathbf{B}_1{}^T \tag{82}$$

Table 1
Four Choices of a Subpreconditioner

	Diagonal, equation (80)	ICF, equation (81)
Block diagonal, equation (77)	No.1	No.2
Lower block triangular, equation (78)	No.3	No.4

Note. ICF = incomplete cholesky factorization.

Therefore, we have the following four types of subpreconditioner that will be tested, as are listed in Table 1.

Before we select a most effective subpreconditioner for the dynamic rupture problem, we first test the four subpreconditioners on the saddle point system given by the time-independent part (i.e., excluding the first two terms on the left hand side) of equation (49), which describes a static or quasi-static dislocation problem; this is reasonable as the dynamic problem is equivalent to a sequence of static problems after time discretization; for simplicity, friction is also removed (i.e., $\mu_f = 0$) during the test. To this end, a simple model is constructed and discretized in space; the resulting linear system is preconditioned using the four subpreconditioners and solved with the GMRES solver with the same parameters; the normalized time for converging at the same tolerance is 0.01, 1.00, 0, and 0.87 for subpreconditioners No.1–No.4. We therefore adopt the block structure of subpreconditioner No.3 for constructing a counterpart for the dynamic problem. For a detailed description of this test, which is also calibrated against an analytical solution given by Pollard and Segall (1987), see the supporting information.

Finally, by extension, we arrive at the following nonstationary (left) subpreconditioner, specific to time step $(n + 1)$ and Newton iteration step $(k + 1)$, that is *best* suited for solving the dynamic rupture problem due to the same fluid effect (equation (61) using the GMRES solver.

$$\widehat{\mathbf{P}}_t^{(n+1,k)} = \begin{bmatrix} \widehat{\mathbf{A}}^{(n+1,k)} & \mathbf{0} \\ \mathbf{B}_2 & \mathbf{B}_2\left(\widehat{\mathbf{A}}^{(n+1,k)}\right)^{-1}{\mathbf{B}_1}^{T(n+1,k)} \end{bmatrix} \tag{83}$$

Here by examining equations (56), (66)–(69), and (73)–(82), we obtain the following forms of the relevant matrices:

$$\widehat{\mathbf{A}}^{(n+1,k)} = (1+\alpha_1 a)\mathrm{lump}(\mathbf{M}) + \alpha_1\,\mathrm{diag}\left(\mathbf{C}^A\right) + (\alpha_1 b + \alpha_2)\,\mathrm{diag}(\mathbf{K}) - \begin{cases} \mathrm{diag}\left(\mathbf{Q}^{(n+1,k)}\right), & \left|\underline{d}^{(n+1,k)}\right| \le d_c/2 \\ \mathbf{0}, & \left|\underline{d}^{(n+1,k)}\right| > d_c/2 \end{cases} \tag{84}$$

$$\mathbf{B}_1^{T(n+1,k)} = \mathbf{J}_{12}^{(n+1,k)} \tag{85}$$

$$\mathbf{B}_2 = \mathbf{J}_{21} \tag{86}$$

In equation (84), $\alpha_1 = 0.5\delta t$, $\alpha_2 = 0.25\delta t^2$, the meaning of $\mathbf{Q}^{(n+1,k)}$ is indicated in equation (66), and the operator *lump* performs lumping of a matrix by summing all the off-diagonal elements in a row to the corresponding diagonal element, such that

$$\mathrm{lump}(\mathbf{M}) = [M_i], M_i = \sum_j M_{ij} \tag{87}$$

While lumping of the mass matrix is usually used in conjunction with explicit time integration schemes or general economy (e.g., Duan & Oglesby, 2006), here, it is performed to maintain the diagonal dominancy of the approximation $\widehat{\mathbf{A}}^{(n+1,k)}$.

Finally, within each Newton iteration step, the iteration of the GMRES solver is terminated when the relative residual of the preconditioned system, defined as below, reaches a predefined tolerance $\mathrm{tol}_{\mathrm{GMRES}}$.

$$r_r{}^{(n+1,k)} = \frac{\left\| \left(\widehat{\mathbf{P}}_t{}^{(n+1,k)}\right)^{-1}\left(-\underline{R}^{(n+1,k)}\right) - \left(\widehat{\mathbf{P}}_t{}^{(n+1,k)}\right)^{-1}\mathbf{J}^{(n+1,k)}\left(\underline{\varsigma}^{(n+1,k+1)} - \underline{\varsigma}^{(n+1,k)}\right) \right\|}{\left\| \left(\widehat{\mathbf{P}}_t{}^{(n+1,k)}\right)^{-1}\left(-\underline{R}^{(n+1,k)}\right) \right\|} \le \mathrm{tol}_{\mathrm{GMRES}} \tag{88}$$

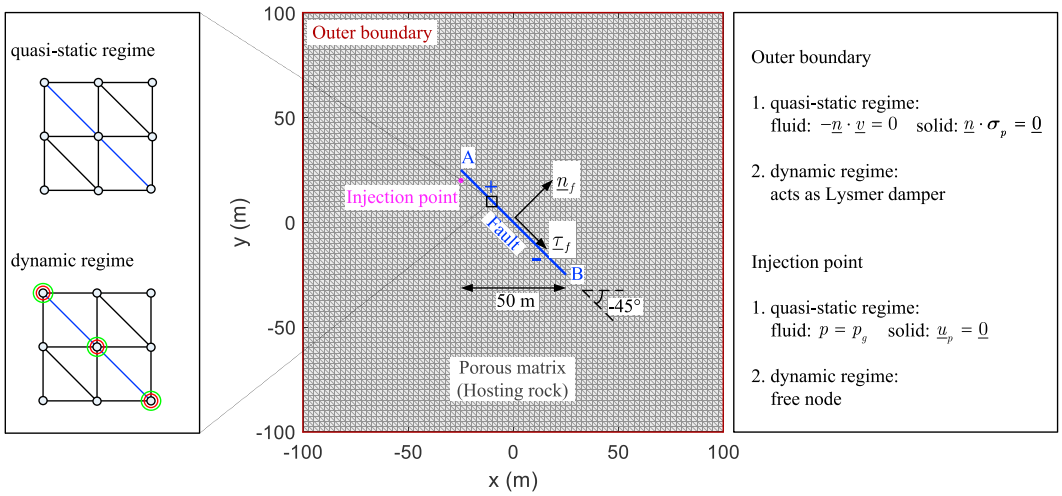

Figure 4. Synthetic model setup: The domain consists of a porous permeable matrix (gray), a hydraulically conductive fault (blue), an injector (magenta) on the fault and an outer boundary (dark red), the latter two subjected to different boundary conditions in the quasi-static and dynamic regimes, as are shown in the box on the right. The mesh used for finite element discretization is also shown. The number of elements is invariant irrespective of the regime of the problem, but the number of nodes differs between the two subproblems. The box on the left illustrates that, in the quasi-static regime, a single layer of fault nodes (black) is used for both the fluid pressure and the solid displacement; in the dynamic subproblem, three coinciding layers of fault nodes (black, red, and green) are used, with two layers for the solid displacement and a third layer for the fault normal contact pressure (i.e., the Lagrangian multiplier).

7. Numerical Example

7.1. Model Setup, Parameters, and Procedures

The synthetic model setup for this numerical exercise is illustrated in Figure 4. A 200 m × 200 m domain is created and is embedded with a fault $50\sqrt{2}$ m long and dipping at $-45°$ at the domain center. The upper left and lower right fault tips are marked with "A" and "B". The positive and negative sides of the fault are marked with "+" and "−". Based on the definition of $\underline{n}_f$ and $\underline{\tau}_f$ shown in Figure 1, $\underline{n}_f$ is $[1,\ 1]^{\mathrm{T}}/\sqrt{2}$ and $\underline{\tau}_f$ is set as $[1,\ -1]^{\mathrm{T}}/\sqrt{2}$. An injector is introduced at $[-25,\ 20$ m] to simulate fluid injection immediately near the fault. In the quasi-static regime, the Dirichlet and Nuemann boundary conditions for both the fluid and the solid are the same as those designed in Jin and Zoback (2017). Specifically, the injection point is subjected to constant injection overpressure p_g for the fluid problem and zero displacement vector for the solid problem; the domain outer boundary is subjected to zero normal fluid flux for the fluid problem and zero traction vector for the solid problem. In the dynamic regime, the Lysmer damper is applied to the domain outer boundary for wave absorption (see section 2.5). The domain is discretized into 12,800 equal-sized linear and isosceles right triangular finite elements with a side length of 2.5 m; a total of 6,561 nodes are generated; the mesh perfectly conforms to the fault, discretizing it into 20 linear line elements (21 nodes). This mesh is used first for the quasi-static subproblem; it is then augmented in the dynamic regime with, (1) additional 21 nodes on the fault via nodal splitting (see Figure 3) to allow for fault slip, resulting in a dual-finite element mesh with 12,800 elements and 6,582 nodes, and (2) another 21 nodes for constructing the discrete Lagrangian space in a manner described in section 5. Note that our computational model is general with respect to the mesh and can operate on an unstructured mesh provided that it conforms to the fault.

For demonstration purposes, the following nominal parameters as are listed in Table 2 are used. In particular, the value of v_u in relation to v is based on Rice and Cleary (1976), as also can be found in Chang and Segall (2016a). The decoupled approach will be employed for including the pore pressure effect, and the coupled approach will be used to account for the poroelastic effect, and the results will be compared. They are hereinafter referred to as the case with pore pressure effect and the case with poroelastic effect, respectively.

Table 2
Model Nominal Parameters

Parameter	Description	Value and unit
quasi-static regime		
ϕ_{m0}	initial matrix porosity	0.2499–0.2501, random
ϕ_{f0}	initial fault porosity	1
C_m	matrix compressibility	1.5×10^{-9} Pa^{-1}
C_f	fault compressibility	1.5×10^{-7} Pa^{-1}
C_ρ	fluid compressibility	5.1×10^{-10} Pa^{-1}
$\boldsymbol{k}_m$	matrix permeability tensor	[1 0; 0 1] mD
b_0	fault initial hydraulic aperture	0.11 mm
η	fluid viscosity	10^{-3} Pa·s
p_g	injection overpressure	5 MPa
s	external fluid source	0
ν	drained Poisson's ratio of the fluid-saturated solid	0.25
α	Biot-Willis coefficient (for the coupled approach only)	0.8
dynamic regime		
ν_u	undrained Poisson's ratio of the fluid-saturated solid	0.30
ρ_0	initial density of the fluid	1,000 kg/m^3
ρ_s	density of the solid mineral	3,000 kg/m^3
μ_s	fault static frictional coefficient	0.600
μ_d	fault dynamic frictional coefficient	0.400
d_c	slip-weakening distance	0.1 mm
a_p	boundary *P* wave absorption coefficient	1
a_s	boundary *S* wave absorption coefficient	1
a	Rayleigh damping coefficient	2
b	Rayleigh damping coefficient	2.0×10^{-3} (within t_c, equation (89))2.0×10^{-5} (beyond t_c, equation (89))
δt	time increment for the dynamic problem	0.1 ms
tol_{NR}	Newton-Raphson solver convergence tolerance	1.0×10^{-6}
$\text{tol}_{\text{GMRES}}$	GMRES solver convergence tolerance	1.0×10^{-9}
general		
E	Young's modulus of the solid	40 GPa
$\boldsymbol{\sigma}_0'$	initial (background) effective stress tensor	[6.0–2.7; −2.7 11.2] MPa

In either case, the numerical solution to the quasi-static subproblem (section 2.3.1) is sought using our Jin and Zoback (2017) computational model. The details are not elaborated here. To provide some physical intuition, we calculate a quantity commonly known as the *hydraulic diffusivity*, defined as $k/(\eta C\phi)$ where k is the permeability along a certain direction, using the parameters provided in Table 2. This yields a 2.7×10^{-3} m^2/s initial matrix diffusivity along both x and y directions and a 6.7 m^2/s initial fault tangential diffusivity. Therefore, qualitatively speaking, the system is *very* diffusive. From $\boldsymbol{\sigma}_0'$, the initial stress state on the fault is calculated, leading to t_{0n}=5.9 MPa, $t_{0\tau}$=2.6 MPa, and CS(t = 0)= − 0.94 MPa. By design, p_g is below t_{0n} such that no hydraulic fracturing occurs. This is because we wish to model only mode-II failure. The time increment for the quasi-static subproblem is set to be 20,000 s.

In parallel to the quasi-static modeling, we track the evolution of CS for determining the transition into the dynamic regime following section 2.3.2. Once t^* is determined, the quasi-static modeling ceases. We then carry out the following few intermediate steps:

1. Extract $p(\underline{x}, t^*)$ as an input for computing $\rho_{\text{mix}}(\underline{x}, t^*)$; extract $p_f(\underline{x}, t^*)$, $t_{p\tau}(\underline{x}, t^*)$, and $t_{pn}(\underline{x}, t^*)$ as inputs for computing the external nodal force vector (equation (54)).
2. Compute $\rho_{\text{mix}}(\underline{x}, t^*)$ following equations (12)–(15) as an input for the mass matrix (equation (50)).
3. Compute $\overline{\rho}_{\text{mix}}(t^*)$, $\overline{V}_p(t^*)$, and $\overline{V}_s(t^*)$ as inputs for the Lsymer damper (equation (51)).
4. Compute all matrices and vectors stated by equations (50)–(54) and (56) for each finite element using the provided parameters.
5. Assemble all global matrices and vectors on the split-node finite element mesh (prepared in advance) following the standard subroutines.

6. Determine the slip direction from equation (21), which yields $\underline{\tau}_s=[-1, 1]^T/\sqrt{2}$ as the unit slip direction vector on the negative side.

Upon completion of the above steps, we then seek for the numerical solution of the dynamic subproblem following the detailed procedures shown in sections 3.3 and 4–6. In this study, we do not explicitly model the nucleation period of quasi-static slip that precedes the dynamic rupture under slip weakening and fluid overpressure (Garagash & Germanovich, 2012). Instead, we artificially nucleate the rupture by prescribing a small increment Δt_τ (i.e., overstress) to the fault shear traction (e.g., Galis et al., 2014). Specifically, Δt_τ is superposed onto $t_{0\tau}$ in the case with pore pressure effect and $t_{0\tau}+t_{p\tau}(\underline{x},t^*)$ in the case with poroelastic effect. We also smooth Δt_τ in time following some standard procedures (e.g., Duru & Dunham, 2016). It reads

$$\Delta t_\tau = \Delta t_{\tau 0}\cdot\begin{cases}\exp\left(\dfrac{(t_d-t_c)^2}{t_d(t_d-2t_c)}\right), 0<t_d<t_c\\ 1, t_d\geq t_c\end{cases} \tag{89}$$

where t_c is a finite time interval over which the overstress is smoothed, $t_d \coloneqq t-t^*$ is the elapsed time since the beginning of the rupture, and $\Delta t_{\tau 0}$ is the maximum magnitude of the overstress. In either case, we choose t_c=0.004 s and $\Delta t_{\tau 0}$=0.1 MPa for meaningful comparisons.

In space, the overstress is enforced on both sides of the fault over a finite nucleation patch around the location on the fault where the Coulomb stress first reaches 0 (hypocenter). Here we prescribe the overstress over the so-called critical patch size (i.e., minimum earthquake size) for physical instability (i.e., nucleation), which is given by

$$L_c=\frac{Ed_c}{2(1+\nu_u)(1-\nu_u)(\mu_s-\mu_d)}\cdot\begin{cases}\dfrac{1}{\min(t_{0n}-p_f(\underline{x},t*))}, \text{pore pressure effect}\\ \dfrac{1}{\min\left(t_{0n}+t_{pn}(\underline{x},t*)\right)}, \text{poroelastic effect}\end{cases}, \underline{x}\in\partial f \tag{90}$$

Equation (90) is adapted from the classic expression of the critical patch size for an in-plane (plane strain) fault shear problem under slip weakening and with homogenous peak and residual strengths along the fault; the expression is independent of the initial fault stress (e.g., Dunham, 2007; Uenishi & Rice, 2003). In our case, we use the undrained Poisson's ratio; because of the heterogeneity in the pore pressure and the poroelastic stress on the fault, we use the minimum difference between the peak and the residual strengths, leading to a conservative estimation of L_c. Note that to implement the nucleation numerically, one needs only to slightly modify the residual vectors (equations (63) and (64)); the Jacobian matrices (equations (65)–(69)) remain unchanged. Preliminary tests reveal that a slip-weakening distance d_c down to 0.1 mm can be sufficiently resolved to allow for the nucleation in the two cases with the fluid effect. We also note that the selection of element size allows for sufficiently resolving the slip-weakening zone (i.e., cohesive zone), which is recommended to be at least 4 times the element size (Day et al., 2005). In our case, this ratio is approximately 4 and 9, respectively, for the cases with pore pressure effect and poroelastic effect.

As for the time increment, notice that we have implemented an implicit time integration scheme, the CFL constraint (section 3.3), which reads $\delta t<\delta h_{\min}/V_p$ in the context of 1-D seismic wave propagation and is a necessary condition for convergence for any explicit time stepping scheme, is not required in in our computational model. On the other hand, the stability criterion of the Newmark family method, which reads $\delta t\leq 2/(\omega\sqrt{1-4\beta})$ where ω is the modal frequency and β is an implementation-specific constant, can pose restrictions on the time increment. However, we have opted for β = 1/4 for the time discretization (see equations (58)–(60)) and the stability is unconditionally met irrespective of δt. In theory, our computational model permits the use of relatively large time steps (relative to a simulated duration of dynamic changes). In our example, given the small domain of focus and only a 50 ms simulated duration of seismic wave propagation (most waves get absorbed at the boundary when t_d>50 ms), we set δt at 0.1 ms.

To highlight the fluid effect, a reference case is also constructed to simulate a seismic event due to a typical tectonic loading path and without the fluid effect (i.e., no density alteration and no fluid modification to the

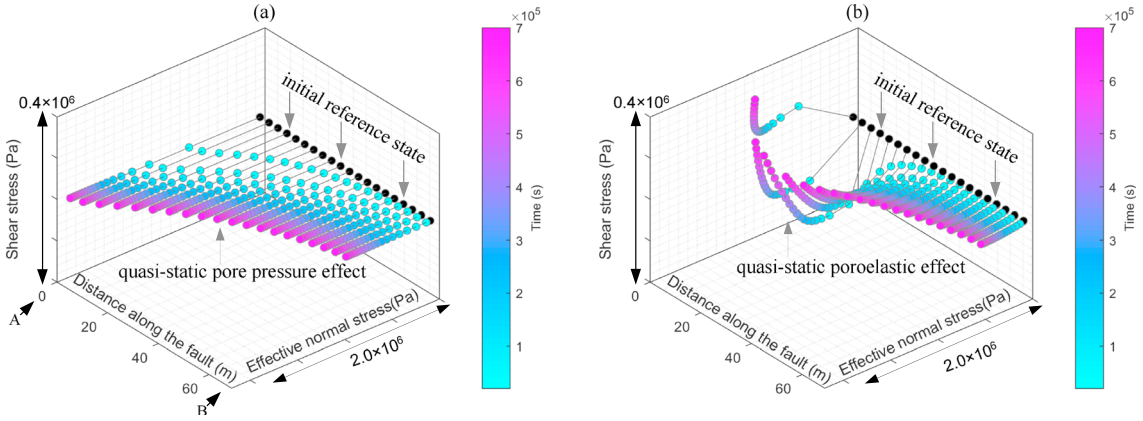

Figure 5. Quasi-static stress paths toward dynamic shear failure. (a) The case with pore pressure effect and (b) the case with poroelastic effect. The initial reference stress state is indicated by the black dots, which is homogenous along the fault, and the time since the beginning of injection is indicated by the color. In both Figures 5a and 5b, 20 stress paths corresponding to the centers of 20 fault elements are plotted, showing heterogeneity along the fault. The distance along the fault is measured from fault tip A to B shown in Figure 4. The shear failure lines (peak strength of the fault) are not shown.

fault stress before rupture). For meaningful comparisons, the same model parameters (2), nucleation parameters in equations (89) and (90), and δt are used. It turns out, however, the corresponding L_c resulted from d_c = 0.1 mm is slightly insufficient to nucleate the rupture. We therefore use a marginally larger nucleation patch size, $n_h \delta h_{\min}$, where $\delta h_{\min}$ = 2.5 m is the minimum finite element size and n_h is constant. We find that n_h = 4 suffices for nucleation. Outside the nucleation patch, a uniform driving shear stress 0.0465 MPa is prescribed on the rest of the fault.

Our computational model is centered around including the fluid effect into dynamic rupture. Currently, calibration of our full-physics model is perhaps not feasible due to the lack of other similar models. Nevertheless, to gain confidence in our numerical solutions, we calibrate a *reduced* version of our computational model by running the benchmark example *tpv12-2d* provided in the repository of the Southern California Earthquake Center/U.S. Geological Survey Spontaneous Rupture Code Verification Project (Harris et al., 2009). All fluid-related additions are removed from the fully discrete form of equations. Our solutions are compared with the *aagaard.2* solutions. Details of the calibration are provided in the supporting information.

7.2. Results

7.2.1. Quasi-Static Stress Path Toward Dynamic Failure

Figure 5 shows the quasi-static fluid effect in initiating the dynamic rupture, which is reflected differently for the case with pore pressure effect (Figure 5a) and the case with poroelastic effect (Figure 5b). In Figure 5a, the stress paths are straight, and the deviation from the initial reference state suggests the amount of pore pressure; in Figure 5b, however, the stress paths are bended owing to the development of additional poroelastic shear stress. The Coulomb stress of each fault element at each time step, as calculated from equation (5) in Figure 5a and equation (6) in Figure 5b, is checked, and the initiation of the dynamic rupture is determined according to equations (7) and (8), leading to t^* = 55.56 hr due to pore pressure effect and t^* = 183.33 hr due to poroelastic effect. In either case, it is shown that the Coulomb stress of the finite element nearest the fault tip A (see Figure 4) reaches 0 first, and therefore, a finite-sized nucleation patch is prescribed on the fault near this element following the procedures described in section 7.1. Figures 5a and 5b also evidently show that the delayed poroelastic triggering is due to the nonlinear stress path (associated with, e.g., the fault tip A) that is bended away from the static failure line starting around 28 hr.

7.2.2. Pressure and Stress at t^*

Figure 6 shows the spatial distribution of the fluid pressure change (Figures 6a and 6c) and of the Coulomb stress (Figures 6b and 6d) in the bulk and at the onset of rupture, t^*, in the case with pore pressure effect (Figures 6a and 6b) and the case with poroelastic effect (Figures 6c and 6d). For the latter case, the corresponding poroelastic fields at t^* are detailed in Figure 7. Figures 6a and 6c serve as inputs for calculating the density, $\rho_{\text{mix}}(\underline{x}, t^*)$, of the fluid-saturated solid at t^*, which is a critical input for the subsequent dynamic rupture modeling; for the case with poroelastic effect, a poroelastic displacement field is further required (see

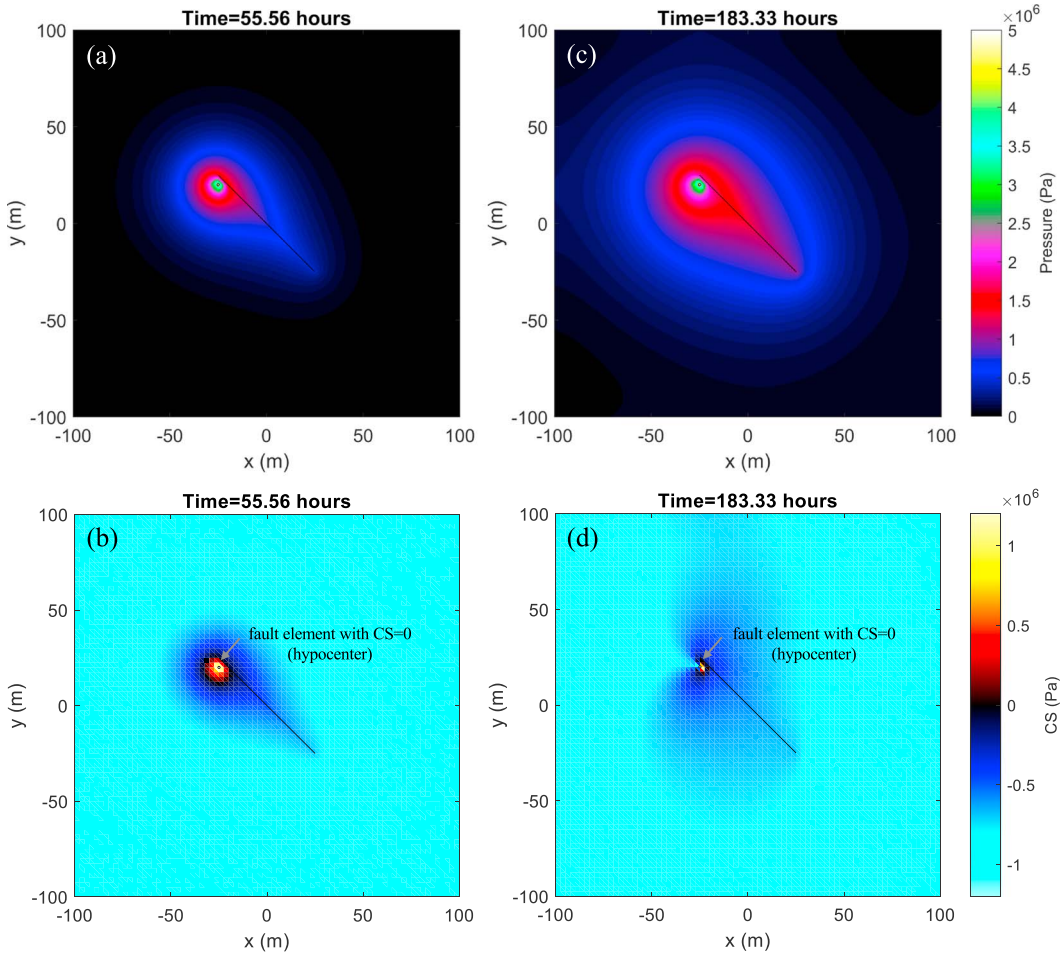

Figure 6. Snapshots of the spatial distribution of the pore pressure change, p (Figures 6a and 6c), and of the Coulomb stress, CS (Figures 6b and 6d), at t^*. The case with pore pressure effect and the case with poroelastic effect are shown in Figures 6a and 6b and in Figures 6c and 6d, respectively, and t^* is indicated at the top of each plot. In all plots, a linear color scale is used. In Figures 6a and 6c, the maximum value on the color bar indicates the simulated injection overpressure, p_g; in Figures 6b and 6d, warm color and cool color indicate positive and negative CS, respectively. Note that on the fault, the maximum CS is 0 and the center of the corresponding fault element is the hypocenter.

Figure 7a). Figure 6a is also used to obtain Figure 6b following equation (5), whereas Figure 6c, together with Figures 7b–7d, is used for arriving at Figure 6d following equation (6). Due to poroelastic coupling, the distributions of the pressure and the Coulomb stress at the time of rupture onset are radically different between the two cases. Specifically for the Coulomb stress, the difference is attributed to not only different changes in the effective normal stress (Figures 7b and 7c) but also the additional shear stress (Figure 7d). On the fault, the fluid pressure and the fault normal traction and shear traction are extracted for the dynamic rupture modeling, as described in section 7.1. Details on the evolution of the fluid pressure and the Coulomb stress in both cases are provided in the supporting information.

Figure 7 shows the spatial distribution of the poroelastic displacement (Figure 7a) and the associated stress tensor (Figures 7b–7d) at t^* for the case with poroelastic effect. Notice that the injector is fixed in both x and y directions, and the outer boundary is subjected to a zero-traction boundary condition (Figure 4) in this example. Although not plotted here, results from earlier time steps reveal that the displacement is most prominent in the area immediately off and surrounding the injector, exhibiting a radial outward expansion; correspondingly, the poroelastic normal stresses are also radially symmetric with respect to the injector and the poroelastic shear stress distributes in symmetric quadrants. However, due to the presence of the highly diffusive fault, the radial pattern changes progressively toward what is shown by Figure 7, where the domain expands outward away from the fault that behaves as a line source (Figure 7a), and the stress tensor is *bended* toward

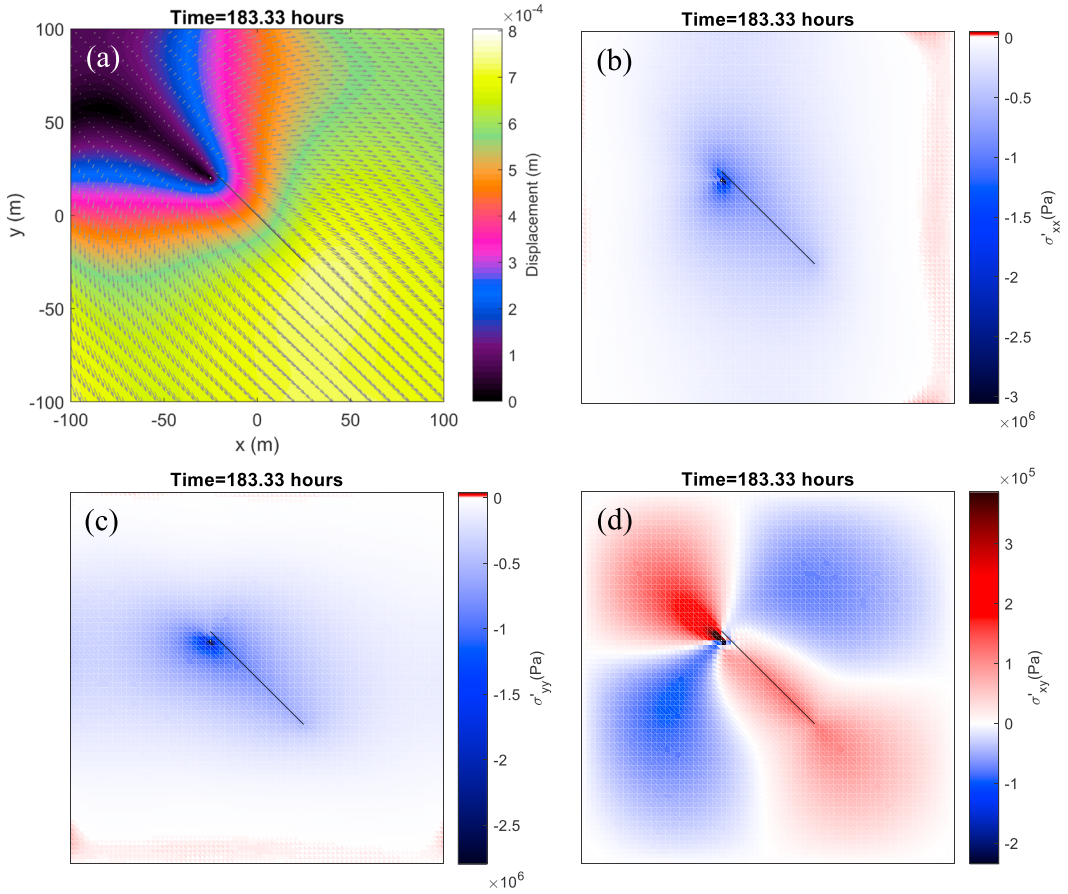

Figure 7. Poroelastic fields at t^* for the case with poroelastic effect. (a) Displacement (color indicates magnitude, and vectors indicate directions), (b) effective normal stress along x, (c) effective normal stress along y, and (d) shear stress. In Figures 7b and 7c, cool color indicates extensional stress (expected in the near field) whereas warm color indicates compressive stress (expected in the far field). t^* is shown at the top of each plot. In Figures 7a–7c, notice that the displacement and the stress tensor are *bended* toward the fault compared to an otherwise radial distribution resulted from a point injection without the fault; similarly, in Figure 7d, the two quadrants experiencing negative shear stress are *pulled* toward the fault and the magnitude differs on the two sides of the fault.

the fault (Figures 7b–7d). Notice also the asymmetry in the shear stress on the two sides of the fault in Figure 7d. Nevertheless, the poroelastic stress is the most prominent surrounding the injector and second near the fault. Details on the evolution of the three components of the poroelastic stress tensor are provided in the supporting information.

7.2.3. Mixture Density at t^*

Figure 8a shows the spatial distribution of the initial reference density, $\rho_{\text{mix0}}(\underline{x})$, of the fluid-solid mixture, calculated according to equations (12)–(15) by setting the pressure change $p(\underline{x}, t^*)$ to zero in equation (13) and by using the first equation in equation (14). The porosity provided in Table 2 is generated following a uniform random distribution between 0.2499 and 0.2501, leading accordingly to the uniform random distribution of $\rho_{\text{mix0}}(\underline{x})$ between 2,499 and 2,501 kg/m^3. The relative change at t^*, that is, $\rho_{\text{mix}}(x, t^*) - \rho_{\text{mix0}}(\underline{x})$, in the cases with pore pressure effect and in the case with poroelastic effect, is shown by Figures 8b and 8c, respectively, where $\rho_{\text{mix}}(x, t^*)$ is again calculated from equations (12) to (15). In both cases, the mixture density undergoes a reduction most noticeably surrounding the injector and near the fault; the distribution of the relative change correlates with the change in the fluid pressure shown in Figures 6a and 6c. Notice that, however, in the latter, the pore volume expansion is due to jointly the pore pressure increase and the poroelastic dilatation shown in Figure 7a.

7.2.4. Coseismic Dynamic Rupture and Wave Propagation

Our computational model exhibits excellent convergence behaviors, see section A3. Figures 9–11 depict the rupture process and the associated spatial-temporal evolution of the coseismic wavefield, specifically, the

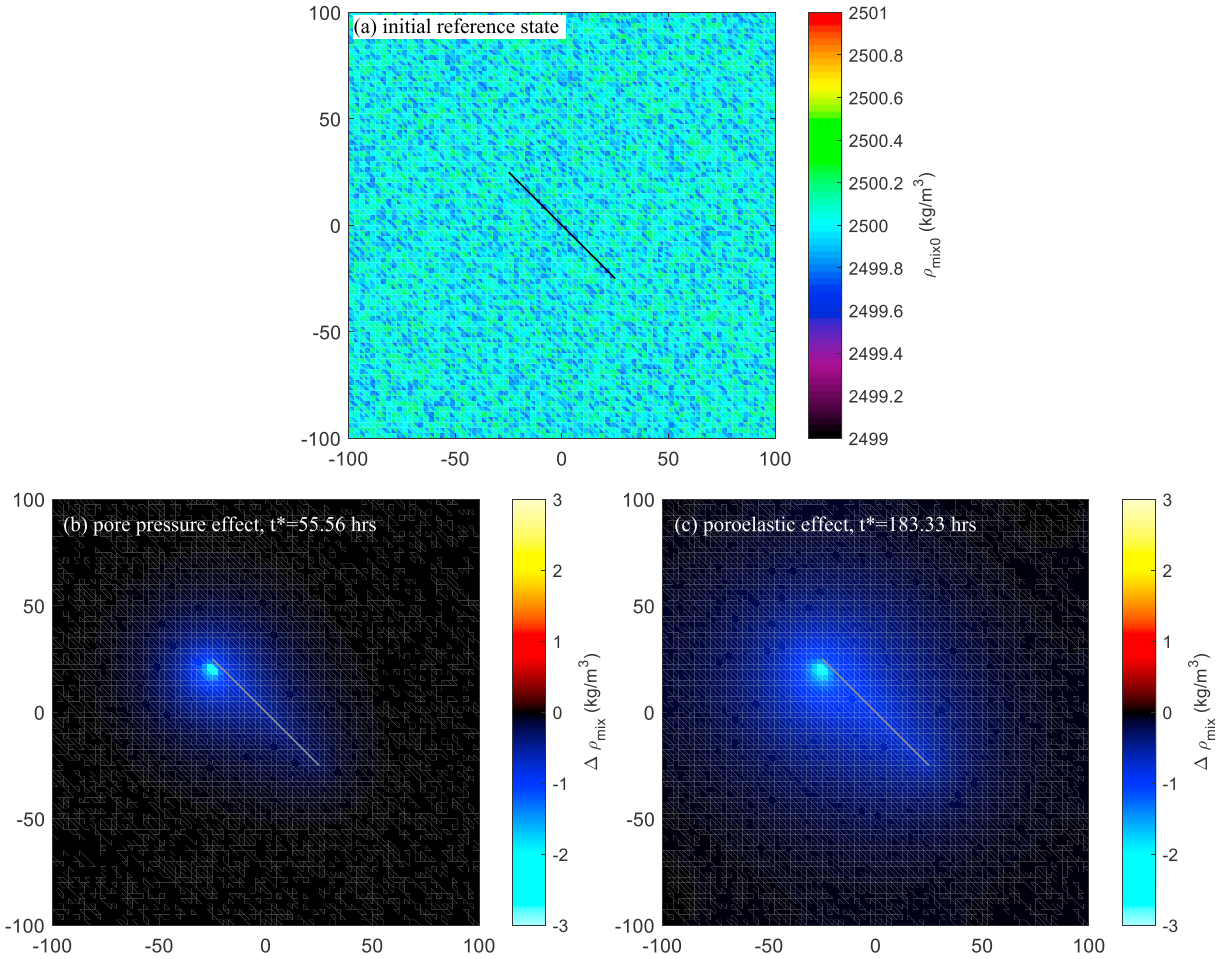

Figure 8. Snapshot of the spatial distribution of the density of the fluid-solid mixture (the fluid-saturated solid). (a) The initial reference state before injection and (b and c) change in the mixture density relative to Figure 8a in the case with pore pressure effect and in the case with poroelastic effect, plotted at their respective *t**. In Figure 8a, the density is random, as calculated from the random distribution of the porosity. In both Figures 8b and 8c, cool color indicates reduction whereas warm color indicates increase; here the mixture density decreases in the area surrounding the injector and the highly diffusive fault, due to an increase in the pore volume and the fluid volumetric fraction (a decrease in the solid volumetric fraction).

magnitude of the particle velocity, from three stages, including an early stage between 4 and 8 ms (Figure 9), an intermediate stage between 11 and 24 ms (Figure 10), and a later stage between 25 and 45 ms (Figure 11). In Figures 9–11, the reference case is shown on the left (Figures 9a–9d, 10a–10d, and 11a–11d), the case with pore pressure effect is shown in the middle (Figures 9e–9h, 10e–10h, and 11e–11h), and the case with poroelastic effect is shown on the right (Figures 9i–9l, 10i–10l, and 11i–11l).

From Figures 9a to 9d, one observes a complete rupture nucleation process in the reference case, where the reverberations over the prescribed nucleation patch decay with time while the rupture front develops and becomes increasingly visible. Comparing Figures 9e and 9i with Figure 9a, one sees that in the two cases with the fluid effect, the required nucleation patch is smaller in size and the nucleation process appears to be longer in time. This is especially the case in the case with poroelastic effect. Nevertheless, once the rupture front picks up, the waves associated with the rupture are significantly stronger in the two cases with the fluid effect, as can be seen from Figures 9f to 9h and 9j to 9l when compared to Figures 9b–9d. In particular, the case with pore pressure effect sees the strongest waves and the case with poroelastic effect yields intermediate results. Such differences manifest themselves as the rupture continues along the rest of the fault (Figure 10) and when the rupture reaches the end of the fault and the wave continues into the rest of the domain (Figure 11). In terms of the rupture velocity, we observe that the rupture propagates at the sub-Rayleigh speed (for the most part) in the reference case but at supershear speed in the two cases

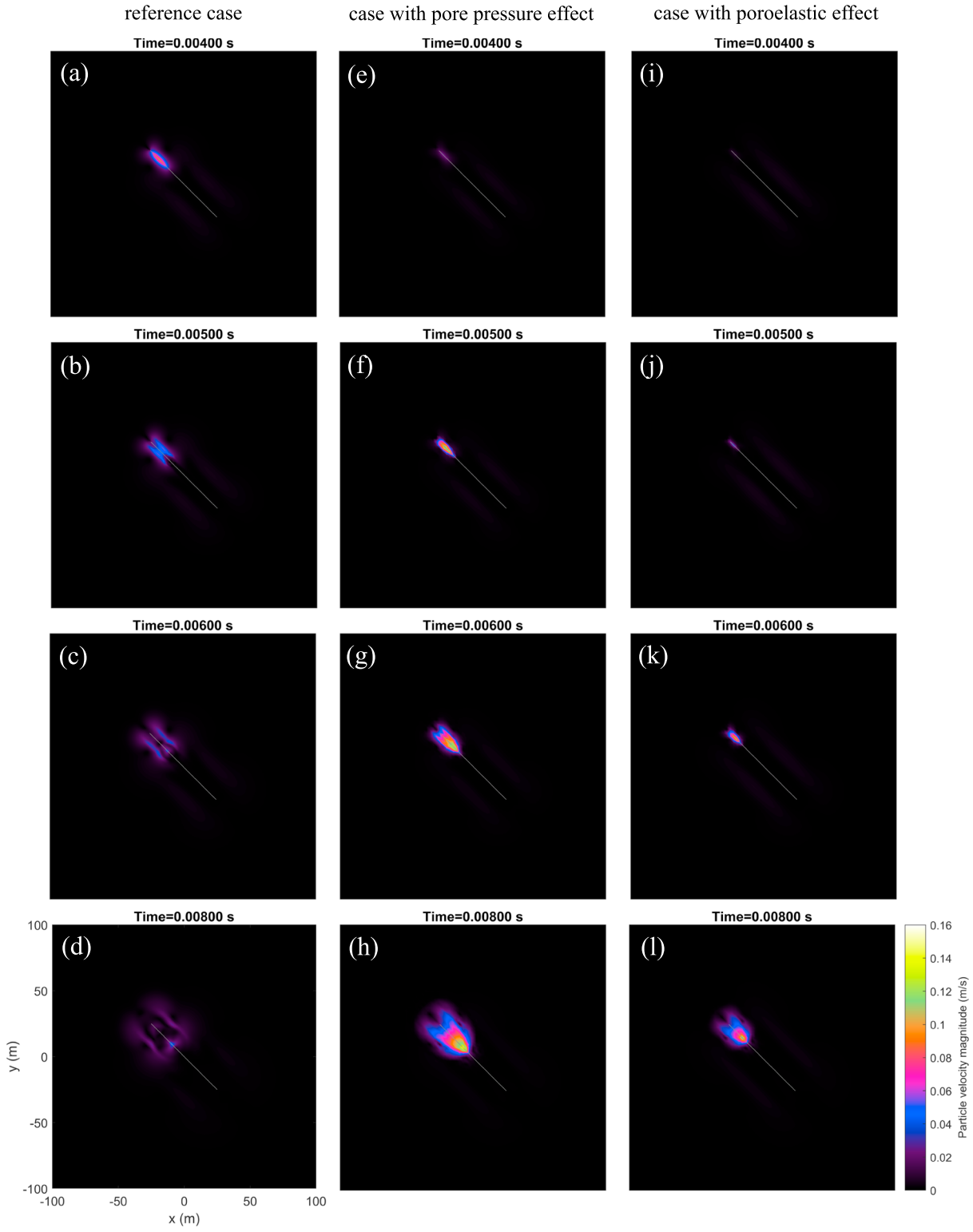

Figure 9. Snapshots of the spatial distribution of the magnitude of the particle velocity at four selected time steps from the early stage of the dynamic modeling showing the nucleation process and rupture front development. The time indicated at the top of each plot refers to t_d (see equation (89)). (a–d) The reference case, (e–h) the case with pore pressure effect, and (i–l) the case with poroelastic effect.

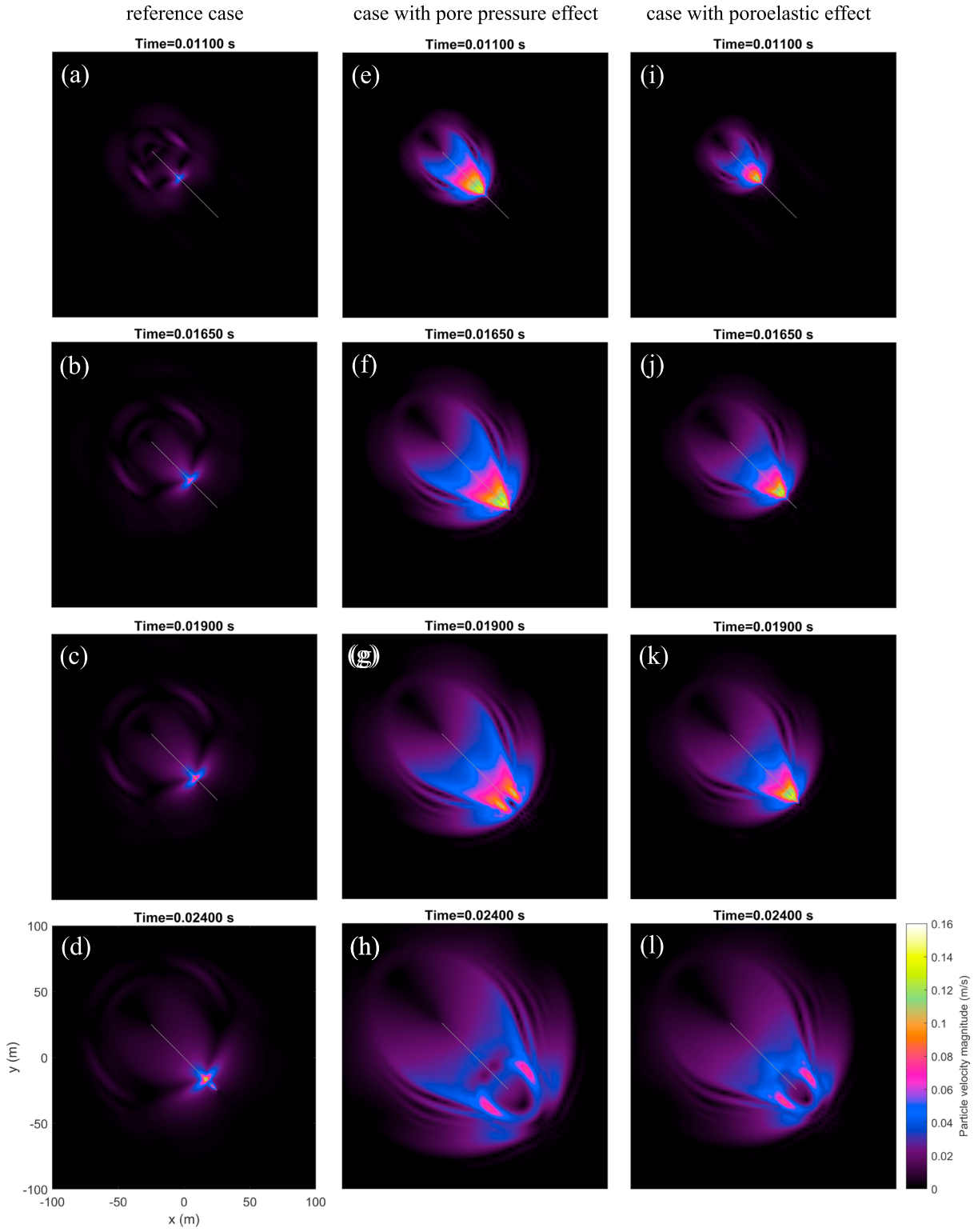

Figure 10. Snapshots of the spatial distribution of the magnitude of the particle velocity at four selected time steps from the intermediate stage of the dynamic modeling showing rupture propagation along the fault. The time indicated at the top of each plot refers to t_d (see equation (89)). (a–d) The reference case, (e–h) the case with pore pressure effect, and (i–l) the case with poroelastic effect.

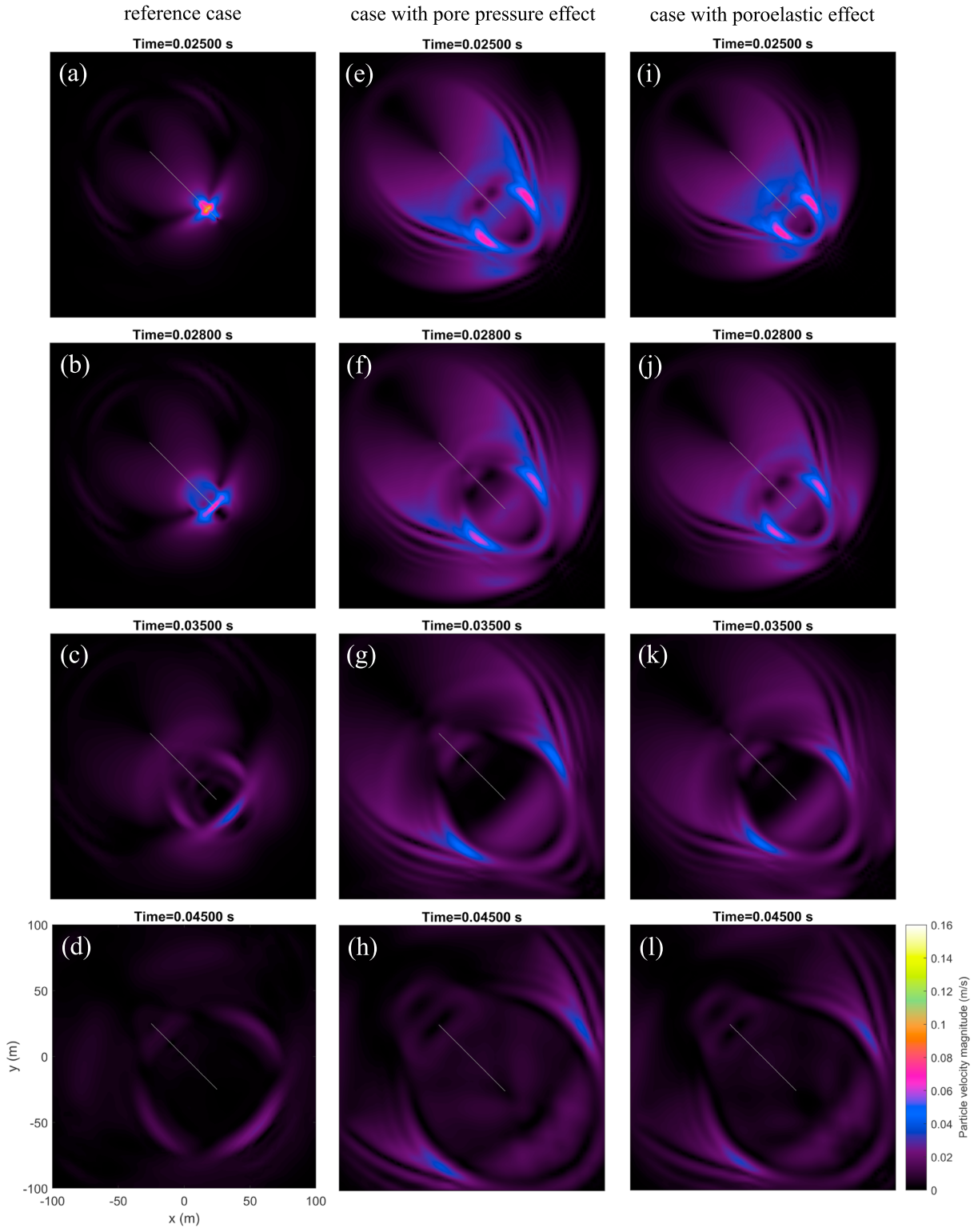

Figure 11. Snapshots of the spatial distribution of the magnitude of the particle velocity at four selected time steps from the later stage of the dynamic modeling showing the wave propagation into the rest of the domain. The time indicated at the top of each plot refers to t_d (see equation (89)). (a–d) The reference case, (e–h) the case with pore pressure effect, and (i–l) the case with poroelastic effect. Notice the absorption of the waves at the domain boundary, in particular Figures 11h and 11l.

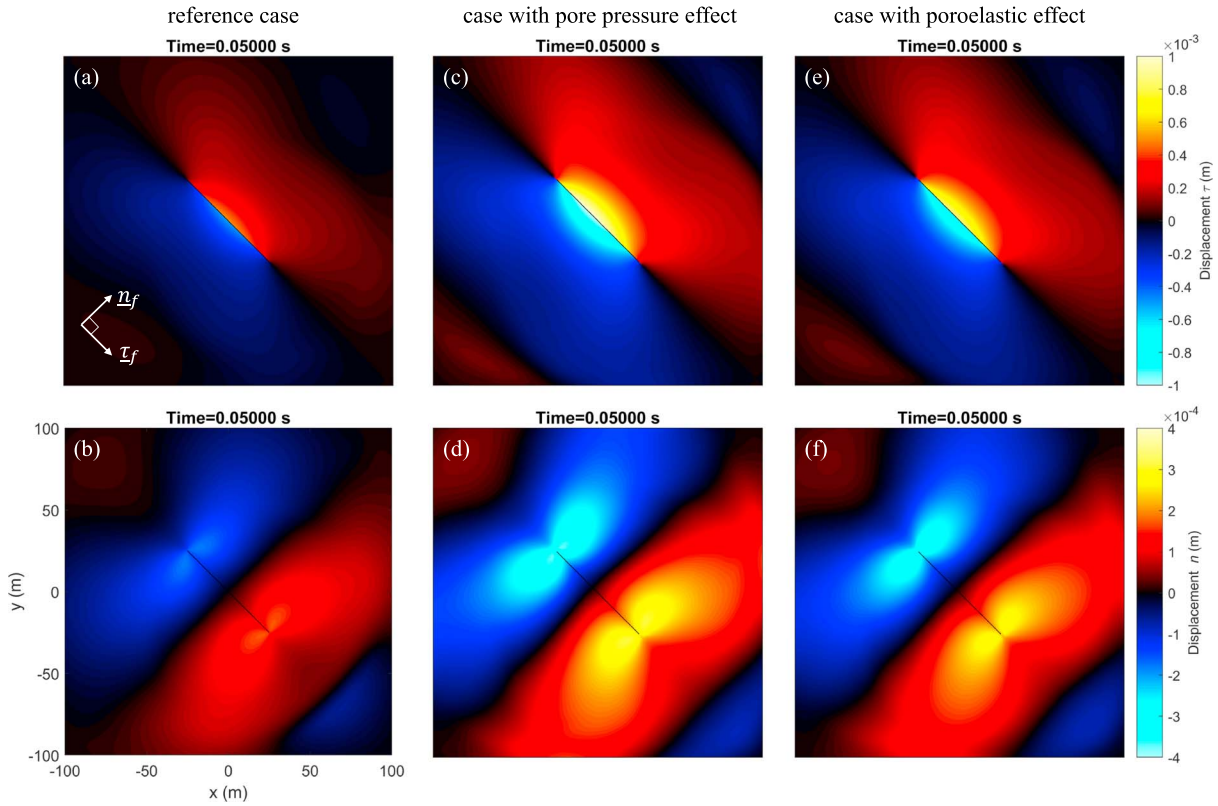

Figure 12. Snapshots of the spatial distribution of the slip-induced displacement, u_s, at the end of the dynamic modeling, in the reference case (Figures 12a and 12b), the case with pore pressure effect (Figures 12c and 12d), and the case with poroelastic effect (Figures 12e and 12f). (a, c, and e) Fault tangential component along τ_f, and (b, d, and f) fault normal component along n_f. In all figures, warm color and cool color indicate positive and negative values, respectively. The time indicated at the top of each plot is t_d.

with the fluid effect; in particular, the case with pore pressure effect sees the fastest rupture velocity that is near the average *P* wave velocity at the onset of rupture, $\overline{V}_p(t^*)$ (see equation (30)), and the case with poroelastic effect sees a rupture velocity between $\overline{V}_p(t^*)$ and $\overline{V}_s(t^*)$. The modeled radiation patterns of both the sub-Rayleigh shear and the supershear resemble some laboratory observations (Xia et al., 2004). Figures 10d, 10f, and 10k, in particular, show the wavefield at the time when the rupture tip reaches the end of the fault in each case. Interestingly and specific to the reference case, Figure 10d captures a transition from the sub-Rayleigh rupture to the supershear rupture, as has also been documented by laboratory studies (e.g., Xia et al., 2004) and numerical exercise (Gabriel et al., 2012). The details on the rupture velocity and the rupture style, which are highly dependent on the stress profile along the fault (section 1), among other factors, are not elaborated here but will be presented in our following paper. Nonetheless, the above observations highlight the critical importance of preserving the fluid effect in the dynamic modeling of induced seismic events. For a view of more time slices, see the supporting information.

7.2.5. Slip-Induced Displacement

Figure 12 shows the spatial distribution of the fault-tangential component (Figures 12a, 12c, and 12e) and the fault-normal component (Figures 12b, 12d, and 12f) of the slip-induced displacement at the end of simulation (t_d = 50 ms). From left to right are the results from the reference case, the case with pore pressure effect and the case with poroelastic effect. The reference case and the case with pore pressure effect yield the least and the most amount of displacement, respectively, and the case with poroelastic effect produces intermediate results, highlighting the importance of accurately resolving the fluid effect. Note that the superposition of Figures 12e and 12f onto Figure 7a gives the final displacement in the case with poroelastic effect.

8. Summary and Conclusion

We have developed a model of coseismic fully dynamic spontaneous fault rupture resulted specifically from the preseismic quasi-static loading exerted by fluid perturbations in a faulted porous medium. The fluid effect was resolved using our Jin and Zoback (2017) model, in a fluid-solid decoupled manner as solely the pore pressure effect and in a fluid-solid fully coupled manner as the poroelastic effect. The latter has not been included in current dynamic rupture models. In our work the poroelastic effect is carried over into the dynamic regime for the first time: it enters the model formulation through (1) the fault boundary condition (i.e., the consistency condition) by modifying the fault traction at the onset of rupture and (2) the fluid-solid mixture density by changing the fluid and solid volumetric fractions. The former has a fundamental control of the rupture style, rupture velocity, and coseismic waves, and the latter is critical for a fully dynamic system with inertia. The above two, together with the time of transition from the quasi-static regime to the fully dynamic regime as well as the location on the fault where the rupture nucleates, necessitate a careful modeling of the spatial-temporal evolution of the pressure, deformation, and stress in the quasi-static regime. In the dynamic regime, the other modeled physics includes fault slip weakening, Rayleigh damping within the bulk, and absorbing boundaries. The fault surface contact constraint was imposed exactly (as opposed to approximately) via the Lagrangian multiplier method.

As for seeking numerical solutions, we referred the readers to our Jin and Zoback (2017) computational model for the quasi-static subproblem; in the presented work, we focused exclusively on the discretization of the dynamic model and the development of computational procedures. The dynamic subproblem was discretized and interpolated in space using a split-node finite element method; a discrete Lagrangian space coinciding with the discretized fault was constructed for interpolating the Lagrangian multiplier while allowing for inf-sup stability. In time, the model was discretized using an implicit and unconditionally stable Newmark family finite difference method. This use of this method removes the CFL constraint and allows for relatively large time steps; however, it also renders the problem highly nonlinear in the presence of slip weakening. We therefore developed a Newton-Raphson solver for solving the fully discrete nonlinear system, which no longer exhibits a symmetric block structure as is typically resulted from most explicit rupture models. Accordingly, we opted for a GMRES iterative solver for solving the final linearized system. To accelerate the convergence, we have also developed a novel physics-based nonstationary preconditioner, which takes outputs from the dynamically evolving Jacobian submatrix and is further approximated with a subpreconditioner. Throughout the numerical formulation, we demonstrated the importance of considering the fluid effect as it systematically modifies the discretized system and the preconditioner and in different manners when being resolved as pore pressure effect or poroelastic effect.

Our Jin and Zoback (2017) computational model provides a tool to examine the triggering mechanism of fluid-induced seismicity in faulted porous media. The computational model presented here is complementary and offers an avenue to study the associated dynamic rupture process. We have demonstrated that the fluid effect can fundamentally alter the coseismic rupture style and wavefield. In our numerical example, the rupture can propagate at supershear speed rather than sub-Rayleigh speed, and the associated wavefield can be significantly stronger in amplitude and dramatically different in radiation pattern than that without including the fluid effect; a more profound postrupture displacement field is also observed. Such findings have important implications for distinguishing induced earthquakes from natural tectonic events. Additionally, we have shown that by resolving the fluid effect as either pore pressure effect or poroelastic effect can lead to marked differences in not only the time of onset of rupture but also, more importantly, the coseismic dynamic changes. For instance, the presented numerical example indicates that by resolving the fluid effect as pore pressure effect rather than poroelastic effect can potentially lead to an overprediction in the rupture speed and the magnitudes of the particle velocity and the postrupture displacement. This therefore highlights the importance of accurately resolving the fluid effect in studying fluid-induced earthquakes. The presented numerical example serves as a simple illustration on the importance of considering the fluid effect. We are currently utilizing this computational model to study in detail the possible impact of fluid effect on coseismic rupture style (particularly, supershear rupture) and its sensitivity to mixture density, fault fluid pressure, and fault poroelastic stress. Finally, we point out that the same computational model can also be applied to study depletion-induced earthquakes that are commonly observed in hydrocarbon reservoirs.

Nomenclature

1. Domain, boundary and fault	
Ω, Ω_m,Ω_f	model domain, matrix domain, fault domain
$\partial\Omega$	domain boundary
$\partial\Omega_p$,$\partial\Omega_v$	fluid Dirichlet boundary, fluid Neumann boundary
$\partial\Omega_u$,$\partial\Omega_t$	solid Dirichlet boundary, solid Neumann boundary
∂f,$\partial f^{\pm}$	fault surface, fault surface on positive and negative sides
$\underline{n}$, $\underline{\tau}$	unit normal and tangential vectors of the domain boundary
$\underline{n}_f^{\pm}$, $\underline{\tau}_f^{\pm}$	unit normal and tangential vectors of fault surfaces on positive and negative sides
$\underline{n}_f$, $\underline{\tau}_f$	unit normal and tangential vectors of the fault, defined as $\underline{n}_f^-$, $\underline{\tau}_f^-$
$\underline{e}_1$,$\underline{e}_2$	unit vector along x and y axes
$\underline{x}$	location within the domain
2. Time	
t	elapsed time since the beginning, s
t^*	time when the dynamic rupture begins, s
t_d	elapsed time since the beginning of rupture, s
t_c	a finite time interval for smoothing nucleation overstress, s
3. Fluid	
p	fluid pressure, Pa
p_f	fluid pressure on the fault, Pa
p_g	fluid Dirichlet boundary value (injection overpressure), Pa
p_s	slip-induced change in the fluid pressure, Pa
ϕ_{mo},ϕ_{fo}	initial intrinsic porosities of the matrix and the fault, [−]
Φ	partial porosity (porosity of the matrix-fault system), [−]
$\overline{\Phi}$	partial porosity modified due to solid-to-fluid coupling, [−]
Λ_0	geometry parameter, [−]
C_m, C_f, C_ρ	compressibility of the matrix, the fault, and the fluid, Pa^{-1}
η	fluid viscosity, Pa·s
$\mathbf{k}_m$	matrix permeability tensor, m^2
b,b_0	fault hydraulic aperture and its initial value, m
$\underline{v}$	flow velocity, m/s
ρ, ρ_0	fluid density and its initial value, kg/m^3
s	external fluid source/sink divided by the initial fluid density, s^{-1}
4. Solid (general)	
E	Young's modulus of the solid, Pa
ρ_s	density of the solid mineral, kg/m^3
μ_s,μ_d	static and dynamic frictional coefficients of the fault, [−]
d_c	slip-weakening distance, m
γ	a parameter describing the relationship between the displacement vectors on the two sides of the fault, [−]
β	an intermediate parameter related to γ
α_f,	an intermediate parameter related to slip weakening, m^{-1}
$\boldsymbol{\sigma}_0$	initial effective stress tensor, Pa
t_{0n},$t_{0\tau}$	initial normal traction and shear traction on the fault, Pa
CS, CS_{max}	Coulomb stress on the fault and its maximum value, Pa
$\mathbf{1}$	unit identity tensor (Kronecker delta), [−]
5. Solid (preseismic, drained)	
ν ,	drained Poisson's ratio of the fluid-saturated solid, [−]
$\boldsymbol{\sigma}_p$,$\boldsymbol{\sigma}_p$	injection-induced poroelastic effective stress tensor and Cauchy total stress tensor, Pa
t_{pn},$t_{p\tau}$	injection-induced normal traction and shear traction on the fault, Pa
$\underline{u}_p$	injection-induced poroelastic displacement, m
6. Solid (coseismic, undrained)	
ν_u	undrained Poisson's ratio of the fluid-saturated solid, [−]
ρ_{mix}	density of the fluid-solid mixture (fluid-saturated solid), kg/m^3
$\overline{\rho}_{mix}$	spatially averaged density of the fluid-solid mixture (fluid-saturated solid), kg/m^3
$\mathbb{C}_u$	undrained elastic stiffness tensor of the fluid-saturated solid under plane strain, Pa
μ_f,	dynamically evolving frictional coefficient of the fault, [−]
$\boldsymbol{\sigma}_s$,$\boldsymbol{\sigma}_s$	slip-induced effective stress tensor and Cauchy total stress tensor, Pa

$\boldsymbol{\sigma}_s^{\pm}$	slip-induced Cauchy total stress tensor on the two sides of the fault, Pa
$\underline{t}_s^{\pm}$	slip-induced traction vector on the two fault surfaces, Pa
$\underline{t}_s$	slip-induced traction vector on the fault, defined as $\underline{t}_s^{-}$, Pa
t_{sn}	slip-induced normal traction on the fault (contact pressure), Pa
$t_{s\tau}$	slip-induced shear traction on the fault, Pa
$\underline{\tau}_s$	unit vector along the direction of slip on the negative side of the fault, [−]
$\underline{u}_s$	slip-induced coseismic displacements, m
$\underline{u}_s^{\pm}$	slip-induced coseismic displacements on the two fault surfaces, m
$\underline{s}$	fault slip vector, m
$\underline{t}_a$	an equivalent traction vector on the absorbing boundary, Pa
$\overline{V}_p, \overline{V}_s$	average P and S wave velocities in the fluid-saturated solid, m/s
a_p, a_s	degree of absorption of P and S waves on the absorbing boundary, [−]
a, b	Rayleigh damping coefficients, [−]
Δt_τ, $\Delta t_{\tau 0}$	(shear) overstress for nucleation and its maximum value, Pa
L_c	critical patch size for nucleation, m
7. Coupling	
α	Biot-Willis coefficient, [−]
8. Variational formulation, discretization, and Newton iteration	
$\varphi, \underline{\eta}$	virtual contact pressure, virtual displacement
$\widehat{\zeta}, \underline{c}$	nodal virtual contact pressure, nodal virtual displacement
$\widehat{l}, \underline{d}$	nodal contact pressure (Lagrangian multiplier), nodal displacement
$\widetilde{l}, \underline{\widetilde{d}}$	intermediate predictions of $\widehat{l}, \underline{d}$
$\widehat{v}_l, \underline{v}_d$	speed of change in the nodal contact pressure and the nodal particle velocity
$\widehat{v}_l, \underline{\widetilde{v}}_d$	intermediate predictions of $\widehat{v}_l, \underline{v}_d$
$\widehat{a}_l, \underline{a}_d$	acceleration of change in the nodal contact pressure and the nodal particle acceleration
$\underline{\varsigma}$	a collectively written unknown vector,$(\underline{a}_d, \widehat{a}_l)$
$\mathbf{N}$	interpolation function associated with 2-D elements
$\underline{N}_l$	interpolation function associated with 1-D elements in the discrete Lagrangian space
$\underline{N}_f$	interpolation function associated with 1-D fault elements
$\mathbf{B}$	displacement-strain transformation matrix
$\mathbf{M}$	mass matrix
$\mathbf{K}$	stiffness matrix
$\mathbf{G}$	contact matrix
$\mathbf{C}^A$	damping matrix due to the absorbing boundary condition
$\mathbf{C}^R$	Rayleigh damping matrix
$\underline{F}$	external nodal force driving/resisting rupture
$\mathbf{J}$	Jacobian matrix
$\mathbf{J}_{11}, \mathbf{J}_{12}, \mathbf{J}_{21}, \mathbf{J}_{22}$	Jacobian submatrices
$\underline{R}$	residual vector
$\underline{R}_d, \underline{R}_l$	residual subvectors
$\mathbf{Q}$	an intermediate output matrix from the Jacobian as an input for the preconditioner
$\underline{e}_d$	a vector composed of unit subvectors specifying the direction of nodal displacements
δt	time increment for the dynamic rupture subproblem, s
tol_{NR}	Newton-Raphson solver convergence tolerance
$(n), (n+1)$	subscripts indicating current and next time steps
$(k), (k+1)$	Subscripts indicating current and next Newton iteration steps
9. Preconditioner and linear iterative solver	
$\mathbf{A}, \mathbf{B}_1^T, \mathbf{B}_2$	(1,1), (1,2), and (2,1) block submatrices of the coefficient matrix subjected to preconditioning
$\mathbf{L}, \mathbf{D}, \mathbf{U}$	matrices obtained from a standard block triangular **LDU** factorization
$\mathbf{S}$	Schur complement
$\widehat{\mathbf{A}}, \widehat{\mathbf{S}}$	approximations of **A**and **S**
$\mathbf{D}'$	a variation of **D**
$\mathbf{P}, \mathbf{P}_d, \mathbf{P}_t$	preconditioner, block-diagonal preconditioner, block-triangular preconditioner
$\widehat{\mathbf{P}}_d, \widehat{\mathbf{P}}_t$	block-diagonal subpreconditioner, block-triangular subpreconditioner
r_r	relative residual of the preconditioned system
$\text{tol}_{\text{GMRES}}$	GMRES solver convergence tolerance

Appendix A

A1. Finite Element Discretization Matrices and Vectors

N is defined in x, while $\underline{N}_f$ and $\underline{N}_l$ are defined along the fault tangential direction. The relevant element-wise matrices take the following forms:

$$\mathbf{N} = \begin{bmatrix} N_1(\underline{x}) & 0 & N_2(\underline{x}) & 0 & N_3(\underline{x}) & 0 \\ 0 & N_1(\underline{x}) & 0 & N_2(\underline{x}) & 0 & N_3(\underline{x}) \end{bmatrix} \tag{A1}$$

$$\underline{N}_f = (N_{f1}(\tau), N_{f2}(\tau)) \tag{A2}$$

$$\underline{N}_l = (N_{l1}(\tau), N_{l2}(\tau)) \tag{A3}$$

$$\mathbf{B} = \begin{bmatrix} N_{1,x} & 0 & N_{2,x} & 0 & N_{3,x} & 0 \\ 0 & N_{1,y} & 0 & N_{2,y} & 0 & N_{3,y} \\ N_{1,y} & N_{1,x} & N_{2,y} & N_{2,x} & N_{3,y} & N_{3,x} \end{bmatrix} \tag{A4}$$

The undrained elastic stiffness matrix under a plane strain condition reads

$$\mathbb{C}_u = \frac{E}{(1+\nu_u)(1-2\nu_u)} \begin{bmatrix} 1-\nu_u & \nu_u & 0 \\ \nu_u & 1-\nu_u & 0 \\ 0 & 0 & (1-2\nu_u)/2 \end{bmatrix} \tag{A5}$$

The element-wise displacement and normal contact pressure (Lagrangian multiplier) take the following forms

$$\underline{d} = \left(d_{1x}, d_{1y}, d_{2x}, d_{2y}, d_{3x}, d_{3y}\right)^T \tag{A6}$$

$$\widehat{l} = (l_1, l_2)^T \tag{A7}$$

A2. Details on Deriving The Jacobian Submatrices

In deriving the Jacobian submatrices according to equation (65), the following expressions are encountered during the intermediate steps.

$$\frac{\partial \underline{F}\left(\underline{d}^{(n+1,k)}, \widehat{l}^{(n+1,k)}\right)}{\partial \underline{a}_d^{(n+1,k)}} = \frac{\partial \underline{F}\left(\underline{d}^{(n+1,k)}, \widehat{l}^{(n+1,k)}\right)}{\partial \left|\underline{d}^{(n+1,k)}\right|} \cdot \frac{\partial \left|\underline{d}^{(n+1,k)}\right|}{\partial \underline{d}^{(n+1,k)}} \frac{d\underline{d}^{(n+1,k)}}{d\underline{a}_d^{(n+1,k)}} \tag{A8}$$

$$\frac{\partial \underline{F}\left(\underline{d}^{(n+1,k)}, \widehat{l}^{(n+1,k)}\right)}{\partial \widehat{a}_l^{(n+1,k)}} = \frac{\partial \underline{F}\left(\underline{d}^{(n+1,k)}, \widehat{l}^{(n+1,k)}\right)}{\partial \widehat{l}^{(n+1,k)}} \frac{d\widehat{l}^{(n+1,k)}}{d\widehat{a}_l^{(n+1,k)}} \tag{A9}$$

$$\frac{\partial |\underline{d}|}{\partial \underline{d}} = \frac{\partial}{\partial \underline{d}}\left[(\underline{d}\cdot\underline{d})^{\frac{1}{2}}\right] = \frac{1}{2}(\underline{d}\cdot\underline{d})^{-\frac{1}{2}}\left(\underline{d}\cdot\frac{\partial \underline{d}}{\partial \underline{d}} + \frac{\partial \underline{d}}{\partial \underline{d}}\cdot\underline{d}\right) = \frac{1}{2}(\underline{d}\cdot\underline{d})^{-\frac{1}{2}} 2\underline{d}\cdot\mathbf{1} = \frac{\underline{d}}{|\underline{d}|} = (\underline{e}_d)_{n\times 1} \tag{A10}$$

$$\frac{d\underline{d}^{(n+1,k)}}{d\underline{a}_d^{(n+1,k)}} = \frac{1}{4}\delta t^2 \mathbf{1}_{n\times n} \tag{A11}$$

$$\frac{d\widehat{l}^{(n+1,k)}}{d\widehat{a}_l^{(n+1,k)}} = \frac{1}{4}\delta t^2 \mathbf{1}_{m\times m} \tag{A12}$$

For an element in contact with a fault element, $\underline{e}_d$ in equation (A10) is composed of three unit vectors specifying the direction of each node. For example, if the first two nodes are fault nodes and the third node is a matrix node, then $\underline{e}_d$ takes the form of

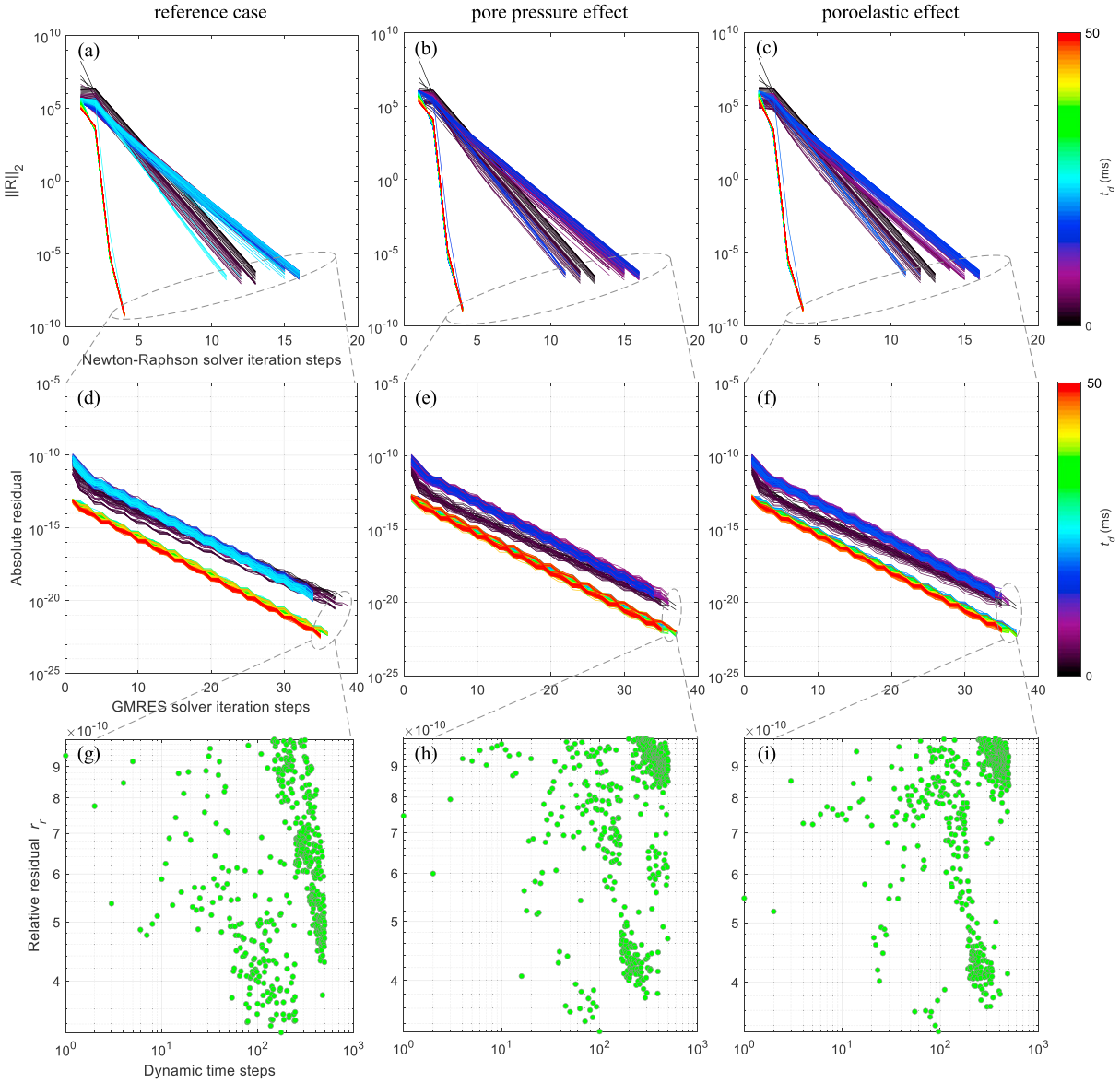

Figure A1. Model convergence in the dynamic regime. (a, d, and g) The reference case, (b, e, and h), the case with pore pressure effect, and (c, f, and i) the case with poroelastic effect. Figures A1a–A1c show the convergence of the outer Newton-Raphson solver at all 500 (dynamic) time steps (the simulated duration of dynamic rupture is 50 ms with $\delta t = 0.1$ ms), where each line represents one time step; as an example, the convergence of the inner iterative GMRES solver at the last Newton-Raphson iteration step for each time step is shown by Figures A1d–A1f, where each line again represents one time step; the relative residual at which the GMRES solver converges at each time step is further shown by Figures A1g–A1i.

$$\underline{e}_d = \left(\tau_{sx}, \tau_{sy}, \tau_{sx}, \tau_{sy}, e_{3x}, e_{3y}\right)^T \tag{A13}$$

where τ_{sx}, τ_{sy} are the components of the slip vector, and e_{3x}, e_{3y} are the components of the unit vector in the direction of the nodal displacement of the third node. In practice, e_{3x}, e_{3y} need not to be known for computing equation (66) as the integration is performed along the fault element only.

From equations (65) and (A8)–(A12), one arrives at the final expressions of the Jacobian submatrices given by equations (66)–(69).

A3. Model Convergence in The Dynamic Regime

Our computational model exhibits excellent convergence behavior at two levels, including the outer Newton-Raphson solver and the inner preconditioned GMRES solvers (see sections 4 and 6), as shown in

Figure A1. The Newton-Raphson solvers converge within 15 iterations at earlier time steps and within 5 iterations toward the end of simulation, as shown by Figures A1a–A1c, where the *y* axis indicates the L_2 norm of the residual vector (equation (62)). Figures A1d–A1f are examples of the convergence of the GMRES solver selected at the last Newton-Raphson iteration step within each time step; the *y* axis is the absolute residual, and the relative residual (equation (88)) is shown in Figures A1h–A1i; the use of the non-stationary preconditioner allows the convergence toward the predefined ultralow tolerance within 40 iterations.

Acknowledgments
This manuscript benefited substantially from insightful conversations with Eric Dunham, Kali Allison, and Norm Sleep. We are grateful to the Associate Editor and the two reviewers for their constructive comments and suggestions that helped improve the quality of this manuscript. We also thank Ossian O'Reilly, Lucile Bruhat, Lanbo Liu, Andreas Krischok, Paul Segall, and Ronaldo Borja for their discussion. Lei Jin is funded by the Stanford Center for Induced and Triggered Seismicity. No data was used in producing this manuscript.

References

Aagaard, B. T., Knepley, M. G., & Williams, C. A. (2013). A domain decomposition approach to implementing fault slip in finite-element models of quasi-static and dynamic crustal deformation. *Journal of Geophysical Research: Solid Earth*, *118*, 3059–3079. https://doi.org/10.1002/jgrb.50217

Ali, S. T. (2014). Defmod-parallel multiphysics finite element code for modeling crustal deformation during the earthquake/rifting cycle. *arXiv preprint arXiv:1402.0429*.

Allison, K. L., & Dunham, E. M. (2017). Earthquake cycle simulations with rate-and-state friction and power-law viscoelasticity. *Tectonophysics*, *733*, 232–256. https://doi.org/10.1016/j.tecto.2017.10.021

Altmann, J. B., Müller, B. I. R., Müller, T. M., Heidbach, O., Tingay, M. R. P., & Weißhardt, A. (2014). Pore pressure stress coupling in 3D and consequences for reservoir stress states and fault reactivation. *Geothermics*, *52*, 195–205. https://doi.org/10.1016/j.geothermics.2014.01.004

Ampuero, J. P., & Ben-Zion, Y. (2008). Cracks, pulses and macroscopic asymmetry of dynamic rupture on a bimaterial interface with velocity-weakening friction. *Geophysical Journal International*, *173*(2), 674–692. https://doi.org/10.1111/j.1365-246X.2008.03736.x

Andrews, D. J. (1976). Rupture velocity of plane strain shear cracks. *Journal of Geophysical Research*, *81*, 5679–5687. https://doi.org/10.1029/JB081i032p05679

Atkinson, G. M. (2015). Ground-motion prediction equation for small-to-moderate events at short hypocentral distances, with application to induced-seismicity hazards. *Bulletin of the Seismological Society of America*, *105*(2A), 981–992. https://doi.org/10.1785/0120140142

Babuška, I. (1973). The finite element method with Lagrangian multipliers. *Numerische Mathematik*, *20*(3), 179–192. https://doi.org/10.1007/BF01436561

Baisch, S., Vörös, R., Rothert, E., Stang, H., Jung, R., & Schellschmidt, R. (2010). A numerical model for fluid injection induced seismicity at Soultz-sous-Forêts. *International Journal of Rock Mechanics and Mining Sciences*, *47*(3), 405–413. https://doi.org/10.1016/j.ijrmms.2009.10.001

Barall, M. (2009). A grid-doubling finite-element technique for calculating dynamic three-dimensional spontaneous rupture on an earthquake fault. *Geophysical Journal International*, *178*(2), 845–859. https://doi.org/10.1111/j.1365-246X.2009.04190.x

Barrett, R., Berry, M., Chan, T. F., Demmel, J., Donato, J., Dongarra, J., & Van der Vorst, H. (1994). Templates for the solution of linear systems: Building blocks for iterative methods. *Society for Industrial and Applied Mathematics*. https://doi.org/10.1137/1.9781611971538

Béchet, É., Moës, N., & Wohlmuth, B. (2009). A stable Lagrange multiplier space for stiff interface conditions within the extended finite element method. *International Journal for Numerical Methods in Engineering*, *78*(8), 931–954. https://doi.org/10.1002/nme.2515

Ben-David, O., Cohen, G., & Fineberg, J. (2010). The dynamics of the onset of frictional slip. *Science*, *330*(6001), 211–214. https://doi.org/10.1126/science.1194777

Benzi, M., Golub, G. H., & Liesen, J. (2005). Numerical solution of saddle point problems. *Acta Numerica*, *14*, 1–137. https://doi.org/10.1017/S0962492904000212

Benzi, M., & Wathen, A. J. (2008). Some preconditioning techniques for saddle point problems. In *model order reduction: Theory, research aspects and applications* (pp. 195–211). Berlin: Springer. https://doi.org/10.1007/978-3-540-78841-6_10

Biot, M. A. (1941). General theory of three-dimensional consolidation. *Journal of Applied Physics*, *12*(2), 155–164. https://doi.org/10.1063/1.1712886

Borja, R. I. (2013). *Plasticity: Modeling & computation*. Berlin: Springer. https://doi.org/10.1007/978-3-642-38547-6

Borja, R. I., & Koliji, A. (2009). On the effective stress in unsaturated porous continua with double porosity. *Journal of the Mechanics and Physics of Solids*, *57*(8), 1182–1193. https://doi.org/10.1016/j.jmps.2009.04.014

Brezzi, F. (1974). On the existence, uniqueness and approximation of saddle-point problems arising from Lagrangian multipliers. *Revue française d'automatique, informatique, recherche opérationnelle. Analyse numérique*, *8*(R2), 129–151. https://doi.org/10.1051/m2an/197408R201291

Brezzi, F., & Bathe, K. J. (1990). A discourse on the stability conditions for mixed finite element formulations. *Computer Methods in Applied Mechanics and Engineering*, *82*(1–3), 27–57. https://doi.org/10.1016/0045-7825(90)90157-H

Buijze, L., van den Bogert, P. A., Wassing, B. B., Orlic, B., & ten Veen, J. (2017). Fault reactivation mechanisms and dynamic rupture modelling of depletion-induced seismic events in a Rotliegend gas reservoir. *Netherlands Journal of Geosciences*, *96*(05), s131–s148. https://doi.org/10.1017/njg.2017.27

Byerlee, J. (1978). Friction of rocks. In *Rock friction and earthquake prediction* (pp. 615–626). Basel: Birkhäuser. https://doi.org/10.1007/978-3-0348-7182-2_4

Cao, H. (2002). Development of techniques for general purpose simulators (Doctoral dissertation, Stanford University).

Cappa, F., & Rutqvist, J. (2012). Seismic rupture and ground accelerations induced by CO_2 injection in the shallow crust. *Geophysical Journal International*, *190*(3), 1784–1789. https://doi.org/10.1111/j.1365-246X.2012.05606.x

Castelletto, N., White, J. A., & Ferronato, M. (2016). Scalable algorithms for three-field mixed finite element coupled poromechanics. *Journal of Computational Physics*, *327*, 894–918. https://doi.org/10.1016/j.jcp.2016.09.063

Catalli, F., Rinaldi, A. P., Gischig, V., Nespoli, M., & Wiemer, S. (2016). The importance of earthquake interactions for injection-induced seismicity: Retrospective modeling of the Basel enhanced geothermal system. *Geophysical Research Letters*, *43*, 4992–4999. https://doi.org/10.1002/2016GL068932

Cesca, S., Rohr, A., & Dahm, T. (2013). Discrimination of induced seismicity by full moment tensor inversion and decomposition. *Journal of Seismology*, *17*(1), 147–163. https://doi.org/10.1007/s10950-012-9305-8

Chang, K. W., & Segall, P. (2016a). Injection-induced seismicity on basement faults including poroelastic stressing. *Journal of Geophysical Research: Solid Earth*, *121*, 2708–2726. https://doi.org/10.1002/2015JB012561

Chang, K. W., & Segall, P. (2016b). Seismicity on basement faults induced by simultaneous fluid injection–extraction. *Pure and Applied Geophysics*, *173*(8), 2621–2636. https://doi.org/10.1007/s00024-016-1319-7

Chang, K. W., & Segall, P. (2017). Reduction of injection-induced pore-pressure and stress in basement rocks due to basal sealing layers. *Pure and Applied Geophysics*, *174*(7), 2649–2661. https://doi.org/10.1007/s00024-017-1567-1

Choo, J., & Borja, R. I. (2015). Stabilized mixed finite elements for deformable porous media with double porosity. *Computer Methods in Applied Mechanics and Engineering*, *293*, 131–154. https://doi.org/10.1016/j.cma.2015.03.023

Cleary, M. P. (1977). Fundamental solutions for a fluid-saturated porous solid. *International Journal of Solids and Structures*, *13*(9), 785–806. https://doi.org/10.1016/0020-7683(77)90065-8

Courant, R., Friedrichs, K., & Lewy, H. (1928). Über die partiellen Differenzengleichungen der mathematischen Physik. *Mathematische Annalen*, *100*(1), 32–74. https://doi.org/10.1007/BF01448839

Cueto-Felgueroso, L., Santillán, D., & Mosquera, J. C. (2017). Stick-slip dynamics of flow-induced seismicity on rate and state faults. *Geophysical Research Letters*, *44*, 4098–4106. https://doi.org/10.1002/2016GL072045

Day, S. M., Dalguer, L. A., Lapusta, N., & Liu, Y. (2005). Comparison of finite difference and boundary integral solutions to three-dimensional spontaneous rupture. *Journal of Geophysical Research*, *110*, B12307. https://doi.org/10.1029/2005JB003813

de la Puente, J., Ampuero, J. P., & Käser, M. (2009). Dynamic rupture modeling on unstructured meshes using a discontinuous Galerkin method. *Journal of Geophysical Research*, *114*, B10302. https://doi.org/10.1029/2008JB006271

Deb, R., & Jenny, P. (2017a). Finite volume–based modeling of flow-induced shear failure along fracture manifolds. *International Journal for Numerical and Analytical Methods in Geomechanics*, *41*(18), 1922–1942. https://doi.org/10.1002/nag.2707

Deb, R., & Jenny, P. (2017b). Modeling of shear failure in fractured reservoirs with a porous matrix. *Computational Geosciences*, *21*(5–6), 1119–1134. https://doi.org/10.1007/s10596-017-9680-x

Deng, K., Liu, Y., & Harrington, R. M. (2016). Poroelastic stress triggering of the December 2013 Crooked Lake, Alberta, induced seismicity sequence. *Geophysical Research Letters*, *43*, 8482–8491. https://doi.org/10.1002/2016GL070421

Dieterich, J. H., Richards-Dinger, K. B., & Kroll, K. A. (2015). Modeling injection-induced seismicity with the physics-based earthquake simulator RSQSim. *Seismological Research Letters*, *86*(4), 1102–1109. https://doi.org/10.1785/0220150057

Duan, B. (2016). Spontaneous rupture on natural fractures and seismic radiation during hydraulic fracturing treatments. *Geophysical Research Letters*, *43*, 7451–7458. https://doi.org/10.1002/2016GL069083

Duan, B., & Oglesby, D. D. (2006). Heterogeneous fault stresses from previous earthquakes and the effect on dynamics of parallel strike-slip faults. *Journal of Geophysical Research*, *111*, B05309. https://doi.org/10.1029/2005JB004138

Dunham, E. M. (2007). Conditions governing the occurrence of supershear ruptures under slip-weakening friction. *Journal of Geophysical Research*, *112*, B07302. https://doi.org/10.1029/2006JB004717

Dunham, E. M., & Rice, J. R. (2008). Earthquake slip between dissimilar poroelastic materials. *Journal of Geophysical Research*, *113*, B09304. https://doi.org/10.1029/2007JB005405

Duru, K., & Dunham, E. M. (2016). Dynamic earthquake rupture simulations on nonplanar faults embedded in 3D geometrically complex, heterogeneous elastic solids. *Journal of Computational Physics*, *305*, 185–207. https://doi.org/10.1016/j.jcp.2015.10.021

El-Abbasi, N., & Bathe, K. J. (2001). Stability and patch test performance of contact discretizations and a new solution algorithm. *Computers & Structures*, *79*(16), 1473–1486. https://doi.org/10.1016/S0045-7949(01)00048-7

Ellsworth, W. L. (2013). Injection-induced earthquakes. *Science*, *341*(6142). https://doi.org/10.1126/science.1225942

Fan, Z., Eichhubl, P., & Gale, J. F. (2016). Geomechanical analysis of fluid injection and seismic fault slip for the M_w4. 8 Timpson, Texas, earthquake sequence. *Journal of Geophysical Research: Solid Earth*, *121*, 2798–2812. https://doi.org/10.1002/2016JB012821

Ferronato, M., Bergamaschi, L., & Gambolati, G. (2010). Performance and robustness of block constraint preconditioners in finite element coupled consolidation problems. *International Journal for Numerical Methods in Engineering*, *81*(3), 381–402.

Ferronato, M., Janna, C., & Gambolati, G. (2008). Mixed constraint preconditioning in computational contact mechanics. *Computer Methods in Applied Mechanics and Engineering*, *197*(45-48), 3922–3931. https://doi.org/10.1016/j.cma.2008.03.008

Gabriel, A. A., Ampuero, J. P., Dalguer, L. A., & Mai, P. M. (2012). The transition of dynamic rupture styles in elastic media under velocity-weakening friction. *Journal of Geophysical Research*, *117*, B09311. https://doi.org/10.1029/2012JB009468

Galis, M., Ampuero, J. P., Mai, P. M., & Cappa, F. (2017). Induced seismicity provides insight into why earthquake ruptures stop. *Science Advances*, *3*(12), eaap7528. https://doi.org/10.1126/sciadv.aap7528

Galis, M., Pelties, C., Kristek, J., Moczo, P., Ampuero, J. P., & Mai, P. M. (2014). On the initiation of sustained slip-weakening ruptures by localized stresses. *Geophysical Journal International*, *200*(2), 890–909.

Garagash, D. I., & Germanovich, L. N. (2012). Nucleation and arrest of dynamic slip on a pressurized fault. *Journal of Geophysical Research*, *117*, B10310. https://doi.org/10.1029/2012JB009209

Gischig, V. S. (2015). Rupture propagation behavior and the largest possible earthquake induced by fluid injection into deep reservoirs. *Geophysical Research Letters*, *42*, 7420–7428. https://doi.org/10.1002/2015GL065072

Givoli, D. (1991). Non-reflecting boundary conditions. *Journal of Computational Physics*, *94*(1), 1–29. https://doi.org/10.1016/0021-9991(91)90135-8

Goertz-Allmann, B. P., & Wiemer, S. (2012). Geomechanical modeling of induced seismicity source parameters and implications for seismic hazard assessment. *Geophysics*, *78*(1), KS25–KS39.

Gritto, R., & Jarpe, S. P. (2014). Temporal variations of Vp/Vs-ratio at The Geysers geothermal field, USA. *Geothermics*, *52*, 112–119. https://doi.org/10.1016/j.geothermics.2014.01.012

Harris, R. A., Barall, M., Archuleta, R., Dunham, E., Aagaard, B., Ampuero, J. P., et al. (2009). The SCEC/USGS dynamic earthquake rupture code verification exercise. *Seismological Research Letters*, *80*(1), 119–126. https://doi.org/10.1785/gssrl.80.1.119

Hazzard, J. F., & Young, R. P. (2004). Dynamic modelling of induced seismicity. *International Journal of Rock Mechanics and Mining Sciences*, *41*(8), 1365–1376. https://doi.org/10.1016/j.ijrmms.2004.09.005

Heinze, T., Galvan, B., & Miller, S. A. (2015). Modeling porous rock fracturing induced by fluid injection. *International Journal of Rock Mechanics and Mining Sciences*, *77*, 133–141. https://doi.org/10.1016/j.ijrmms.2015.04.003

Hughes, T. J. (2012). *The finite element method: Linear static and dynamic finite element analysis*. Englewood Cliffs, NJ: Courier Corporation.

Itasca Consulting Group (1999). *PFC2D (particle flow code in 2 dimensions)*. Minneapolis, MN: Itasca Consulting Group, Inc.

Jha, B., & Juanes, R. (2014). Coupled multiphase flow and poromechanics: A computational model of pore pressure effects on fault slip and earthquake triggering. *Water Resources Research*, *50*, 3776–3808. https://doi.org/10.1002/2013WR015175

Jin, L., & Zoback, M. D. (2017). Fully coupled nonlinear fluid flow and poroelasticity in arbitrarily fractured porous media: A hybrid-dimensional computational model. *Journal of Geophysical Research: Solid Earth*, *122*, 7626–7658. https://doi.org/10.1002/2017JB014892

Juanes, R., Jha, B., Hager, B. H., Shaw, J. H., Plesch, A., Astiz, L., & Frohlich, C. (2016). Were the May 2012 Emilia-Romagna earthquakes induced? A coupled flow-geomechanics modeling assessment. *Geophysical Research Letters*, *43*, 6891–6897. https://doi.org/10.1002/2016GL069284

Kozdon, J. E., Dunham, E. M., & Nordström, J. (2013). Simulation of dynamic earthquake ruptures in complex geometries using high-order finite difference methods. *Journal of Scientific Computing*, *55*(1), 92–124. https://doi.org/10.1007/s10915-012-9624-5

Kroll, K. A., Richards-Dinger, K. B., & Dieterich, J. H. (2017). Sensitivity of induced seismic sequences to rate-and-state frictional processes. *Journal of Geophysical Research: Solid Earth*, *122*, 10,207–10,219. https://doi.org/10.1002/2017JB014841

Ladyzhenskaya, O. A. (1969). *The mathematical theory of viscous incompressible flow* (Vol. 12). New York: Gordon & Breach.

Liu, F., & Borja, R. I. (2010). Stabilized low-order finite elements for frictional contact with the extended finite element method. *Computer Methods in Applied Mechanics and Engineering*, *199*(37-40), 2456–2471. https://doi.org/10.1016/j.cma.2010.03.030

Liu, M., & Gorman, D. G. (1995). Formulation of Rayleigh damping and its extensions. *Computers & Structures*, *57*(2), 277–285. https://doi.org/10.1016/0045-7949(94)00611-6

Lysmer, J., & Kuhlemeyer, R. L. (1969). Finite dynamic model for infinite media. *Journal of the Engineering Mechanics Division*, *95*(4), 859–878.

Maillot, B., Nielsen, S., & Main, I. (1999). Numerical simulation of seismicity due to fluid injection in a brittle poroelastic medium. *Geophysical Journal International*, *139*(2), 263–272. https://doi.org/10.1046/j.1365-246x.1999.00933.x

Majer, E. L., Baria, R., Stark, M., Oates, S., Bommer, J., Smith, B., & Asanuma, H. (2007). Induced seismicity associated with enhanced geothermal systems. *Geothermics*, *36*(3), 185–222. https://doi.org/10.1016/j.geothermics.2007.03.003

McClure, M. W., & Horne, R. N. (2011). Investigation of injection-induced seismicity using a coupled fluid flow and rate/state friction model. *Geophysics*, *76*(6), WC181–WC198. https://doi.org/10.1190/geo2011-0064.1

Megies, T., & Wassermann, J. (2014). Microseismicity observed at a non-pressure-stimulated geothermal power plant. *Geothermics*, *52*, 36–49. https://doi.org/10.1016/j.geothermics.2014.01.002

Meng, C. (2017). Benchmarking Defmod, an open source FEM code for modeling episodic fault rupture. *Computers & Geosciences*, *100*, 10–26. https://doi.org/10.1016/j.cageo.2016.11.014

Mukuhira, Y., Dinske, C., Asanuma, H., Ito, T., & Häring, M. O. (2017). Pore pressure behavior at the shut-in phase and causality of large induced seismicity at Basel, Switzerland. *Journal of Geophysical Research: Solid Earth*, *122*, 411–435. https://doi.org/10.1002/2016JB013338

Murphy, S., O'Brien, G. S., McCloskey, J., Bean, C. J., & Nalbant, S. (2013). Modelling fluid induced seismicity on a nearby active fault. *Geophysical Journal International*, *194*(3), 1613–1624. https://doi.org/10.1093/gji/ggt174

Newmark, N. M. (1959). A method of computation for structural dynamics. *Journal of the Engineering Mechanics Division*, *85*(3), 67–94.

Norbeck, J. H., & Horne, R. N. (2016). Evidence for a transient hydromechanical and frictional faulting response during the 2011 M_w 5.6 Prague, Oklahoma earthquake sequence. *Journal of Geophysical Research: Solid Earth*, *121*, 8688–8705. https://doi.org/10.1002/2016JB013148

Pollard, D. D., & Segall, P. (1987). Theoretical displacements and stresses near fractures in rock: With applications to faults, joints, veins, dikes, and solution surfaces. *Fault Mechanics of Rock*, *277*(349), 277–349.

Raziperchikolaee, S., Alvarado, V., & Yin, S. (2014). Microscale modeling of fluid flow-geomechanics-seismicity: Relationship between permeability and seismic source response in deformed rock joints. *Journal of Geophysical Research: Solid Earth*, *119*, 6958–6975. https://doi.org/10.1002/2013JB010758

Rice, J. R. (1993). Spatio-temporal complexity of slip on a fault. *Journal of Geophysical Research*, *98*, 9885–9907. https://doi.org/10.1029/93JB00191

Rice, J. R., & Ben-Zion, Y. (1996). Slip complexity in earthquake fault models. *Proceedings of the National Academy of Sciences*, *93*(9), 3811–3818. https://doi.org/10.1073/pnas.93.9.3811

Rice, J. R., & Cleary, M. P. (1976). Some basic stress diffusion solutions for fluid-saturated elastic porous media with compressible constituents. *Reviews of Geophysics*, *14*, 227–241. https://doi.org/10.1029/RG014i002p00227

Richards-Dinger, K., & Dieterich, J. H. (2012). RSQSim earthquake simulator. *Seismological Research Letters*, *83*(6), 983–990. https://doi.org/10.1785/0220120105

Riffault, J., Dempsey, D., Archer, R., Kelkar, S., & Karra, S. (2016). Understanding poroelastic stressing and induced seismicity with a stochastic/deterministic model: An application to an EGS stimulation at Paralana, South Australia, 2011. *In Proc. 41st Stanford Workshop on Geothermal Reservoir Engineering*, SGP-TR-209.

Rinaldi, A. P., & Nespoli, M. (2017). TOUGH2-seed: A coupled fluid flow and mechanical-stochastic approach to model injection-induced seismicity. *Computers & Geosciences*, *108*, 86–97. https://doi.org/10.1016/j.cageo.2016.12.003

Schöberl, J., & Zulehner, W. (2007). Symmetric indefinite preconditioners for saddle point problems with applications to PDE-constrained optimization problems. *SIAM Journal on Matrix Analysis and Applications*, *29*(3), 752–773. https://doi.org/10.1137/060660977

Scuderi, M. M., & Collettini, C. (2016). The role of fluid pressure in induced vs. triggered seismicity: Insights from rock deformation experiments on carbonates. *Scientific Reports*, *6*(1), 24852. https://doi.org/10.1038/srep24852

Segall, P. (1985). Stress and subsidence resulting from subsurface fluid withdrawal in the epicentral region of the 1983 Coalinga earthquake. *Journal of Geophysical Research*, *90*, 6801–6816. https://doi.org/10.1029/JB090iB08p06801

Segall, P., & Fitzgerald, S. D. (1998). A note on induced stress changes in hydrocarbon and geothermal reservoirs. *Tectonophysics*, *289*(1-3), 117–128. https://doi.org/10.1016/S0040-1951(97)00311-9

Segall, P., Grasso, J. R., & Mossop, A. (1994). Poroelastic stressing and induced seismicity near the Lacq gas field, southwestern France. *Journal of Geophysical Research*, *99*, 15,423–15,438. https://doi.org/10.1029/94JB00989

Segall, P., & Lu, S. (2015). Injection-induced seismicity: Poroelastic and earthquake nucleation effects. *Journal of Geophysical Research: Solid Earth*, *120*, 5082–5103. https://doi.org/10.1002/2015JB012060

Solberg, J. M., & Papadopoulos, P. (2005). An analysis of dual formulations for the finite element solution of two-body contact problems. *Computer Methods in Applied Mechanics and Engineering*, *194*(25-26), 2734–2780. https://doi.org/10.1016/j.cma.2004.06.045

Stark, M. A., & Davis, S. D. (1996). Remotely triggered microearthquakes at The Geysers geothermal field, California. *Geophysical Research Letters*, *23*, 945–948. https://doi.org/10.1029/96GL00011

Suckale, J. (2009). Induced seismicity in hydrocarbon fields. *Advances in Geophysics*, *51*, 55–106. https://doi.org/10.1016/S0065-2687(09)05107-3

Thomas, M. Y., Lapusta, N., Noda, H., & Avouac, J. P. (2014). Quasi-dynamic versus fully dynamic simulations of earthquakes and aseismic slip with and without enhanced coseismic weakening. *Journal of Geophysical Research: Solid Earth*, *119*, 1986–2004. https://doi.org/10.1002/2013JB010615

Uenishi, K., & Rice, J. R. (2003). Universal nucleation length for slip-weakening rupture instability under nonuniform fault loading. *Journal of Geophysical Research*, *108*(B1), 2042. https://doi.org/10.1029/2001JB001681

Viesca, R. C., & Rice, J. R. (2012). Nucleation of slip-weakening rupture instability in landslides by localized increase of pore pressure. *Journal of Geophysical Research*, *117*, B03104. https://doi.org/10.1029/2011JB008866

Viesca, R. C., Templeton, E. L., & Rice, J. R. (2008). Off-fault plasticity and earthquake rupture dynamics: 2. Effects of fluid saturation. *Journal of Geophysical Research*, *113*, B09307. https://doi.org/10.1029/2007JB005530

Walsh, F. R. III, & Zoback, M. D. (2016). Probabilistic assessment of potential fault slip related to injection-induced earthquakes: Application to north-central Oklahoma, USA. *Geology*, *44*(12), 991–994. https://doi.org/10.1130/G38275.1

Wang, C. Y., & Barbour, A. J. (2017). Influence of pore pressure change on coseismic volumetric strain. *Earth and Planetary Science Letters*, *475*, 152–159. https://doi.org/10.1016/j.epsl.2017.07.034

Wang, H. F. (2000). *Theory of linear poroelasticity*. Princeton, NJ: Princeton University Press.

Wassing, B. B. T., Van Wees, J. D., & Fokker, P. A. (2014). Coupled continuum modeling of fault reactivation and induced seismicity during enhanced geothermal operations. *Geothermics*, *52*, 153–164. https://doi.org/10.1016/j.geothermics.2014.05.001

Wathen, A. (2015). Preconditioning. *Acta Numerica*, *24*, 329–376. https://doi.org/10.1017/S0962492915000021

White, J. A., & Borja, R. I. (2008). Stabilized low-order finite elements for coupled solid-deformation/fluid-diffusion and their application to fault zone transients. *Computer Methods in Applied Mechanics and Engineering*, *197*(49-50), 4353–4366. https://doi.org/10.1016/j.cma.2008.05.015

White, J. A., & Borja, R. I. (2011). Block-preconditioned Newton-Krylov solvers for fully coupled flow and geomechanics. *Computational Geosciences*, *15*(4), 647–659. https://doi.org/10.1007/s10596-011-9233-7

White, J. A., Castelletto, N., & Tchelepi, H. A. (2016). Block-partitioned solvers for coupled poromechanics: A unified framework. *Computer Methods in Applied Mechanics and Engineering*, *303*, 55–74. https://doi.org/10.1016/j.cma.2016.01.008

Xia, K., Rosakis, A. J., & Kanamori, H. (2004). Laboratory earthquakes: The sub-Rayleigh-to-supershear rupture transition. *Science*, *303*(5665), 1859–1861. https://doi.org/10.1126/science.1094022

Yeck, W. L., Weingarten, M., Benz, H. M., McNamara, D. E., Bergman, E. A., Herrmann, R. B., et al. (2016). Far-field pressurization likely caused one of the largest injection induced earthquakes by reactivating a large preexisting basement fault structure. *Geophysical Research Letters*, *43*, 10,198–10,207. https://doi.org/10.1002/2016GL070861

Yoon, J. S., Zang, A., & Stephansson, O. (2014). Numerical investigation on optimized stimulation of intact and naturally fractured deep geothermal reservoirs using hydro-mechanical coupled discrete particles joints model. *Geothermics*, *52*, 165–184. https://doi.org/10.1016/j.geothermics.2014.01.009

Zbinden, D., Rinaldi, A. P., Urpi, L., & Wiemer, S. (2017). On the physics-based processes behind production-induced seismicity in natural gas fields. *Journal of Geophysical Research: Solid Earth*, *122*, 3792–3812. https://doi.org/10.1002/2017JB014003

Zhao, X., & Young, R. P. (2011). Numerical modeling of seismicity induced by fluid injection in naturally fractured reservoirs. *Geophysics*, *76*(6), WC167–WC180. https://doi.org/10.1190/geo2011-0025.1

Zoback, M. D., & Gorelick, S. M. (2015). To prevent earthquake triggering, pressure changes due to CO_2 injection need to be limited. *Proceedings of the National Academy of Sciences*, *112*(33), E4510–E4510. https://doi.org/10.1073/pnas.1508533112

Zoback, M. D., & Zinke, J. C. (2002). Production-induced normal faulting in the Valhall and Ekofisk oil fields. In *The mechanism of induced seismicity* (pp. 403–420). Basel: Birkhäuser. https://doi.org/10.1007/978-3-0348-8179-1_17